Next Materials 10 (2026) 101529

Contents lists available at ScienceDirect

Next Materials

journal homepage: www.sciencedirect.com/journal/next-materials

Research article

Integrating water-exfoliated phosphorene into poly(lactic-co-glycolic) acid: Stability and photoactivity potential

Agata Costanzo [a,1], Carla Caponio [a,2], Serena Coiai [a], Francesca Cicogna [a], Giulia Lorenzetti [a], Emanuela Pitzalis [a], Franco Dinelli [b], Enrico Berretti [c], Stefano Caporali [d], Andrea Pucci [e], Elisa Passaglia [a,*]

[a] CNR-Consiglio Nazionale delle Ricerche, Istituto di Chimica dei Composti OrganoMetallici (ICCOM-CNR), SS di Pisa, Area della Ricerca di Pisa, Italy
[b] CNR-Consiglio Nazionale delle Ricerche, Istituto Nazionale di Ottica (INO-CNR) Area della Ricerca di Pisa, Italy
[c] CNR-Consiglio Nazionale delle Ricerche, Istituto di Chimica dei Composti OrganoMetallici (ICCOM-CNR), Area della Ricerca di Firenze, Italy
[d] UNIFI-Dipartimento di Ingegneria Industriale (DIEF), Firenze, Italy
[e] UNIPI-Dipartimento di Chimica e Chimica Industriale (DCCI), Pisa, Italy

ARTICLE INFO

Keywords:
Black phosphorus (bP)
Water-based exfoliation
2D-bP
PLGA/2D-bP hybrids
Photoactivity

ABSTRACT

In this study, we report the development and comprehensive characterization of novel poly(lactic-co-glycolic acid) (PLGA)-based nanocomposites incorporating phosphorene nanoflakes. Phosphorene was produced by ultrasound-assisted exfoliation of black phosphorus in the presence of sodium dodecyl sulfate (SDS) as a surfactant, and was then subsequently embedded into a PLGA matrix to fabricate phosphorene–PLGA nanocomposite films, prepared here for the first time, and emulsions. The structural, thermal, and photophysical properties of these hybrid materials were systematically investigated, with a focus on the interfacial interactions between the polymer matrix and the 2D nanofillers. The integration of phosphorene nanosheets significantly enhances the thermal stability of PLGA at elevated temperatures (with a notable shift of ~40 °C), while slightly accelerating its hydrolytic degradation at lower temperatures, resulting in a ~20 % reduction in molecular weight. More interestingly, the PLGA matrix plays a protective role, mitigating the degradation of phosphorene during the polymer hydrolytic degradation. Importantly, we study for the first time the photophysical behaviour of phosphorene nanoflakes embedded in PLGA emulsions, highlighting their potential for photodynamic therapy (PDT) applications. While free phosphorene nanoflakes exhibit outstanding photocatalytic activity in generating singlet oxygen, their embedding within PLGA micelles causes a marked suppression (~90 %) of this activity, likely due to restricted oxygen diffusion in the polymeric environment. This previously unreported limitation is crucial for evaluating the applicability of phosphorene–PLGA systems in biomedical contexts, particularly in PDT.

1. Introduction

The direct liquid-phase exfoliation (LPE) of black phosphorus (bP) through ultrasonication is a widely employed method for producing phosphorene nanoparticles (2D-bP) for biomedical applications [1–8]. Suitable solvents for exfoliation are typically aprotic and high-boiling, such as dimethyl sulfoxide (DMSO), N-methyl-2-pyrrolidone (NMP), N-cyclohexyl-2-pyrrolidone (CHP), and N,N-dimethylformamide (DMF). These solvents have surface tension capable of overcoming the energy of van der Waals stacking of bP nanoflakes [9,10], which is relatively high compared to other 2D systems, resulting in high yields of nanoparticles with photoactivity features suitable for applications in photodynamic (PDT) and photothermal (PTT) therapies [9]. They also stabilize the nanoparticles over time, but are toxic to the environment and health and difficult to remove from the 2D-bP surfaces. For biomedical applications, 2D-bP must be resuspended in water or saline,

* Corresponding author.
E-mail addresses: elisa.passaglia@pi.iccom.cnr.it, elisa.passaglia@cnr.it (E. Passaglia).
[1] Present Address: Scuola Superiore Sant'Anna, Centro di Ricerca Interdisciplinare sulla Sostenibilità e il Clima, Via Santa Cecilia, n. 24, 56127, Pisa, Italia and Università di Padova, Dipartimento di Ingegneria Industriale, Via Gradenigo, n. 6a, 35131, Padova, Italia
[2] Present Address: Department of Materials and Environmental Chemistry, Stockholm University, Svante Arrhenius väg 16 C, SE-106 91 Stockholm

https://doi.org/10.1016/j.nxmate.2025.101529
Received 25 February 2025; Received in revised form 23 October 2025; Accepted 8 December 2025

which requires repeated centrifugation and resuspension steps [11–13] leading to decreased concentration [14] and uncertainty about complete solvent removal. On the other hand, when ultrasonication was used to exfoliate bP in water, it did not produce stable 2D-bP. Even though the water surface tension is high enough to allow exfoliation (72 mJ/m^2 while the requested value is about 40 mJ/m^2 [15,16]) and its viscosity and density values are similar to those of the effective solvents, numerous studies have consistently reported low exfoliation yields and poor stabilization performance [9,10,17].

In our recent work, we exfoliated bP in two different solvents: Cyrene, a biobased solvent with potential biomedical applications, and water. Both solvents produced similar results in terms of 2D-bP oxidation stability and photoactivity, specifically in singlet oxygen generation capacity although Cyrene still needs to be removed through washing/centrifugation steps. The exfoliation yields ranged from 1 to 1.5 wt%, under mild experimental conditions, whereby NMP (used as a comparative sonication medium) resulted in a 3 wt% yield [14]. These findings suggest that water can reduce the interlayer van der Waals interactions by penetrating between the bP layers. However, water was unable to produce long-term stable suspensions, leading to rapid sedimentation of nanoparticles within a few days. In addition, 2D-bP is prone to degradation in the presence of oxygen, which is highly soluble in water. This leads to the formation of oxidized species [18], thereby reducing the final concentration of 2D-bP in the aqueous suspension. To stabilize the 2D-bP in water, emulsifiers were used, providing good exfoliation results, controlled nanoflake dimensions with good stability [19,20]. In particular, Hersam et al. reported interesting results about the exfoliation in a water solution containing small quantities of sodium dodecyl sulphate (SDS, 2 wt%, added to deionized and de-aerated water); it was proved that the presence of SDS yielded stable 2D-bP dispersions with high concentration and photophysical features comparable to those of micromechanically exfoliated nanoparticles, suitable for use in field-effect-transistors [19].

SDS is an organic compound widely used as an anionic surfactant in many cleaning and hygiene applications: detergents for laundry, but also as a food additive since it is considered and generally recognized as a safe (GRAS) ingredient, according to the USFDA (21 CFR 172.822) [21]. Furthermore, SDS has many applications in the biomedical field, such as in protein refolding, amyloid fractionation [22], and as an ionic solubilizer and emulsifier to produce creams, lotions, and gels.

To enhance the stability of 2D-bP nanoparticles and shield the surfaces from oxygen degradation, 2D-bP is frequently encapsulated in polymers. Its polymeric nanocomposites and hybrids have been extensively researched for various biomedical applications, including bioimaging, phototherapy, and drug delivery [23]. For these applications, it is crucial to investigate not only the therapeutic performance—such as the effectiveness of drug release and photoinduced antiviral or antibacterial properties—but also how the nanocomposite system is absorbed or degraded within the body. Polymer emulsions or nanocomposites specifically designed for biomedical purposes should be made from biodegradable, biocompatible, and bioresorbable macromolecules. Poly (lactic-co-glycolic acid), PLGA, is a copolymer approved by the Food and Drug Administration (FDA) for applications in therapeutic devices [24] due to its biodegradability and biocompatibility [25]; recently, it was also proposed as a suitable polymeric matrix for the preparation of nanocomposites with exfoliated bP. Wang et al. [26] prepared PLGA microspheres containing $SrCl_2$ and bP nanosheets as near-infrared light-triggered drug delivery platforms for bone regeneration. Kamyar et al. [27] incorporated 2D-bP into PLGA fibers via solution blow spinning to study the release of phosphate ions for bone tissue engineering applications. Chu et al. [28] developed PLGA nanospheres encapsulating bP quantum dots, which demonstrated high photothermal therapy (PTT) efficiency. Combined with the polymer phase's biodegradability and biocompatibility, these nanospheres hold significant promise for clinical applications. All these papers highlight the remarkable performance of the systems, but they generally lack precise structural characterization and in-depth analysis of the potential interactions between the polymer and the 2D-bP, which could significantly impact their ultimate properties.

In our study, bP was initially exfoliated in water with a small amount of SDS (1 wt%) and then embedded or encapsulated in PLGA. The use of aqueous solutions of SDS as a safer, greener, and alternative sonication medium to prepare 2D-bP suspensions is chosen here to overcome the environmental and health challenges related to the currently used organic solvents. The collected 2D-bP nanoparticles were characterized by UV-Vis, Inductively Coupled Plasma Optical Emission (ICP-OES), Raman and X-ray Photoelectron (XPS) Spectroscopies for an in-depth investigation of concentration, structural features and stability over time. Dynamic Light Scattering (DLS), Atomic Force Microscopy (AFM), Scanning Electron Microscopy (SEM), and Transmission Electron Microscopy (TEM) were employed to analyze the average dimensions, size distribution, and morphology of the prepared 2D-bP. Photoactivity and in particular the capability of a water-based 2D-bP suspension to generate singlet oxygen [29] was tested by UV measurements in the presence of a sensitizer (1,3-diphenylisobenzofuran, DPBF) [30].

Furthermore, the nanoparticles were enclosed in nano-sized micelles of PLGA [28], capable of further protecting them from oxidation, coalescence and precipitation phenomena. The emulsion system's morphology and photoactivity were analysed. Additionally, nanocomposites of PLGA with varying amounts and sizes of 2D-bP nanoparticles were prepared for the first time. The nanocomposites were studied to understand the potential interactions between 2D-bP and PLGA macromolecules and their impact on the thermal and hydrolytic stability of the polymer matrix. To achieve this goal, the nanocomposites were thoroughly structurally characterized using infrared (FT-IR), Raman spectroscopies, and Size Exclusion Chromatography (SEC), while their thermal properties were examined using Differential Scanning Calorimetry (DSC) and Thermogravimetric Analysis (TGA).

2. Experimental section

2.1. Materials

Unless otherwise specified, all the materials were used as received without further purification. PLGA, lactide:glycolide ratio 50:50 (product name: Resomer® RG 504 H) (CAS: 26780–50–7), molecular weight (MW) = 38,000–54,000 g/mol, poly(vinyl alcohol) (PVA) (CAS: 9002–89–5), MW= 13,000–23,000 g/mol, and 87–89 % hydrolyzed; SDS ACS reagent, ≥ 99.0 % purity (CAS: 151–21–3), MW= 288.38 g/mol; DPBF, ≥ 96.5 % purity (CAS: 5471–63–6), MW= 270.32 g/mol; chloroform ACS reagent, ≥ 99.8 % purity (CAS: 67–66–3), MW= 119.38 g/mol, and acetone ACS reagent, ≥ 99.5 % purity, (CAS: 67–64–1), MW= 58.08 g/mol, were acquired from Sigma Aldrich.

Ethanol absolute for analysis (CAS: 64–17–5), MW= 46.07 g/mol, was purchased from Supelco-Sigma Aldrich. Dichloromethane (DCM) (CAS 75–09–2), ≥ 99 % purity with ethanol as a stabilizer, MW= 84.93 g/mol, was acquired from Acros Organics.

High-purity bP (99.998 % purity) was sourced from Smart Elements (SKU: 03933).

All suspensions were prepared using deionized ultrapure water (resistivity: 18.2 MOhm cm) obtained using a Milli-Q system (Millipore, Bedford, MA, USA).

2.2. Preparation methods

2.2.1. 2D-bP suspensions

2D-bP suspensions were prepared through liquid-phase exfoliation. In a typical run, microcrystalline bP (~5.0 mg) was introduced in a 20 mL Schlenk flask (subjected to three nitrogen-vacuum cycles) with 5 mL of solvent. A water solution with SDS (1 % wt/vol) and pure water were used as sonication media.

All the liquids used were previously degassed by fluxing nitrogen for

20 min. The suspension was then sonicated for 5 h under an inert atmosphere (nitrogen flow) at a power of 5 W and amplitude of 50 % using an ultrasonic transducer system (Hielscher Ultrasonic Processor (UP220St), equipped with Sonotrode S26d2 probe (diameter: 2 mm; 26 kHz). During the sonication, the Schlenk flask was immersed in an ice bath to avoid the cavitation-induced heating of the suspension. At the end of the sonication, the resulting dark suspension was centrifuged at 7000 rpm for 15 min. The yellowish transparent supernatant was carefully collected, removed and stored in the dark, while the dark powder precipitate was re-suspended in 5 mL of solvent and subjected to additional sonication for 1–5 h. At the end of the sonication, the suspension was centrifuged at 3000 or 7000 rpm for 15 min to obtain a yellowish supernatant, which was again removed and stored in the dark. This procedure yielded stable 2D-bP suspensions, characterized by a reproducible rotation-speed-dependent size distribution. The 2D-bP suspensions were characterized with DLS and UV-Vis absorption spectroscopy.

2.2.2. 2D-bP PLGA/PVA emulsions

PLGA/PVA and 2D-bP PLGA/PVA emulsions were prepared using oil-in-water solvent evaporation, following a protocol reported in literature [28,31]. In the case of the 2D-bP PLGA/PVA sample, briefly, 5 mL of the 2D-bP suspension in water and SDS were centrifuged for 15 min at 14,000 rpm, and the precipitate was redispersed in 1 mL of a PLGA solution in DCM (10 mg/mL). The so obtained organic fraction was sonicated for 5 min, and then it was drop-by-drop added to 10 mL of PVA aqueous solution (0.5 % wt./vol) and sonicated again for 5 min. The emulsion was stirred under nitrogen at room temperature overnight to evaporate the residual DCM. PLGA/PVA emulsion was prepared using the same procedure without 2D-bP.

2.2.3. 2D-bP/PLGA composites

2D-bP/PLGA composites were obtained following an optimized experimental procedure to produce nanocomposites containing 2D-bP particles with different sizes and concentrations (Figure ESI 1). Composites were prepared using 2D-bP obtained through liquid phase exfoliation in SDS/water solutions. Starting from the solid bP, suspended in the SDS aqueous solution and sonicated for five hours, a dark suspension (step 1) was obtained, then centrifuged at 7000 rpm for 15 min (step 2). The supernatant was removed and analyzed with DLS and UV-Vis spectroscopy and then further centrifuged at 14,000 rpm for 15 min (step 3) to precipitate, collect, and use 2D-bP for the preparation of PLGA+bP_1 (step 4). The black- powder of bP precipitated after the centrifugation at 7000 rpm was collected, suspended in degassed water, and sonicated again for one hour (step 5). The dark suspension was then centrifuged at 3000 rpm for 15 min (step 6). The supernatant was removed and centrifuged again at 14,000 rpm for 15 min (step 7) to precipitate and collect 2D-bP to prepare PLGA+bP_2 (step 8). Finally, the 2D-bP precipitated after the centrifugation at 3000 rpm was collected and used to prepare PLGA+bP_3 (step 9).

All composites (PLGA+bP_1, PLGA+bP_2, and PLGA+bP_3) were prepared using a solution mixing and intercalation method. Under a continuous stream of N_2, 100 mg of PLGA were dissolved in 5 mL DCM in a 20 mL Schlenk flask (subjected to three nitrogen-vacuum cycles). Different fractions of 2D-bP obtained as previously described were then added, and the suspension was sonicated for 3–4 min to disperse bP in the polymeric solution. The composites were obtained as polymer films via solvent casting, depositing the mixture on a Teflon support to let the solvent evaporate. Commercial PLGA powder was also used for measurements or analyses as a reference sample.

2.3. Samples characterization

2.3.1. Raman spectroscopy (Raman)

Raman analysis was conducted using a RENISHAW RAMAN inVia system equipped with a Leica DLML optical microscope having a 50x NPLAN objective. The instrument has a diode laser source at $\lambda = 785$ nm and a Nd:YAG $\lambda = 532$ wavelength, respectively with an emission power ranging between 5 % and 10 %. Each measurement involved an acquisition time of 10 s, with five accumulations. The Raman spectra were recorded within the 1000–100 cm^{-1} range. Samples were analyzed in different forms, including polymeric films, powders, and suspensions. For suspension analysis, a few drops of the sample were placed on a glass slide, and the solvent was evaporated in a vacuum oven at 40°C for 30 min.

2.3.2. Fourier-transform infrared spectroscopy (FT-IR)

FT-IR spectroscopy was performed using a Perkin-Elmer Spectrum Two instrument. Spectra were collected at room temperature in the range of 4000–400 cm^{-1} with a resolution of 4 cm^{-1} and 64 accumulations. Samples were analyzed as polymeric films obtained via solution casting by depositing a few drops of a solution (typically in chloroform or dichloromethane) onto a KBr window. The attenuated total reflection (ATR) technique was employed for solid samples (bP precipitates) placed directly onto the diamond crystal.

2.3.3. UV-visible spectroscopy (UV-Vis)

UV-Vis spectral analysis was conducted on suspensions and emulsions using a Jasco V750 double-beam UV–visible spectrophotometer. Spectra were recorded over the 200–900 nm range at room temperature.

2.3.4. Dynamic light scattering (DLS)

DLS measurements were performed on 2D-bP suspensions and emulsions at ambient temperature using a Malvern Zetasizer Nano S (model ZEN1600). This instrument features a He-Ne laser (633 nm, 4 mW) and an avalanche photodiode detector at 173°. The data were processed using Dispersion Technology Software (Malvern Instruments).

2.3.5. Size exclusion chromatography (SEC)

The molecular weight distribution, including number average molecular weight ($\overline{M_n}$), weight average molecular weight ($\overline{M_w}$), dispersity (Đ), was assessed via SEC using an Agilent Technologies 1200 Series system. This setup consisted of a degasser, an isocratic HPLC pump, a refractive index (RI) detector, and two PLgel 5 μm MiniMIX-D columns maintained at 35°C. $CHCl_3$ was employed as the mobile phase at a 0.3 mL/min flow rate. Calibration was performed using polystyrene standards ranging from 500 to 3×10^5 Da. Samples were prepared at ~3 mg/mL in $CHCl_3$ and filtered through a 0.20 μm syringe filter before analysis. Molecular weight calculations were performed using Agilent ChemStation software.

2.3.6. Thermogravimetric analysis (TGA)

TGA measurements were carried out using a Seiko Exstar 7200 TGA/DTA instrument. The sample weights ranged from 3 to 8 mg and were placed in alumina crucibles with a volume of 70 μL. The thermal analysis was performed in a nitrogen (N_2) atmosphere, heating the samples from 30°C to 700°C at 10°C per minute. Both solid nanocomposites and PLGA samples were analyzed.

2.3.7. Differential scanning calorimetry (DSC)

DSC analyses were performed using a Perkin Elmer DSC4000 instrument. Samples (3–6 mg) were sealed in aluminum pans and subjected to heating and cooling cycles between 30 and 180°C at 10 °C/min. Each sample was analyzed in triplicate. The second heating cycle was used to evaluate thermal transitions, with the data processed using PYRIS 9.0.2 software.

2.3.8. Scanning electron microscopy (SEM)

SEM imaging was conducted using an FEI Quanta 450 ESEM FEG with various detectors (SE high vacuum, SE low vacuum, SE environmental, SE compatible for EDXS, STEM, CCD, and a color camera). The system included a Bruker QUANTAX EBSD backscattered electron

diffraction (EBSD) analysis module, a heating cell (T_{max}=1000°C), and a Peltier cooling/heating cell (-25°C to +60°C). Micrographs were acquired from gold-sputtered film surfaces prepared via spin-coating 2D-bP suspensions (centrifuged at 7000 rpm) and emulsions onto Si/SiO_2 wafers. Spin-coating was performed with a POLOS Spin 150i/250i instrument, using 60 μL of suspension or emulsion under the following conditions: 300 rpm for 30 s followed by 3000 rpm for 60 s.

2.3.9. Atomic force microscopy (AFM)

AFM measurements were carried out using a hybrid system consisting of a commercial SMENA head (NT-MDT, Moscow, Russia) integrated with custom electronics and control software. A digital HF2LI lock-in amplifier (Zurich Instruments, Zurich, Switzerland) was used for data acquisition. The instrument operated in tapping mode at room temperature with an HQ:NSC35 cantilever (MikroMasch, Wetzlar, Germany), which has a nominal spring constant of ~5 N/m and a resonance frequency of 150 kHz. Analyses were conducted on films prepared via spin-coating of 2D-bP suspensions (centrifuged at 7000 rpm) and 2D-bP/PLGA emulsions onto Si/SiO_2 wafers, following the procedure mentioned above.

2.3.10. Transmission electron microscopy (TEM)

TEM imaging was performed using an HR-TEM 200 kV ZEISS LIBRA 200 FE (Carl Zeiss AG, Jena, Germany) equipped with a second-generation in-column Ω filter and an HAADF detector. The 2D-bP suspension in H_2O and SDS, initially centrifuged at 7000 rpm, was further centrifuged at 14,000 rpm. The supernatant was removed, and the precipitated flakes were dried in a vacuum oven at 40°C for 30 min. Samples were then redispersed in ethanol, stirred, and deposited on TEM grids, allowing solvent evaporation before analysis.

2.3.11. X-ray Photoelectron Spectroscopy (XPS)

XPS analysis was performed under ultrahigh vacuum (UHV, 10^{-9} mbar) using a VSW HAC 500 hemispherical electron-energy analyzer with a non-monochromatic Mg Kα X-ray source (1.254 keV) operating at 120 W (12 kV × 10 mA). The 2D-bP suspension in H_2O and SDS, previously centrifuged at 7000 rpm, underwent further centrifugation at 14,000 rpm. The supernatant was discarded, and the precipitated flakes were dried in a vacuum oven at 40°C for 30 min. The flakes were then dispersed in 1 mL of degassed ethanol and sonicated for one minute before deposition onto a sample holder using conductive carbon tape. The sample was introduced into the UHV system under an inert N_2 atmosphere and kept in the introduction chamber for at least 24 h before analysis to allow complete solvent evaporation.

2.3.12. Inductively coupled plasma optical emission spectroscopy (ICP-OES)

ICP-OES was employed to determine the concentration of elemental phosphorus in 2D-bP suspensions. A 450 μL sample was dissolved in 2 mL of nitric acid (Fluka, TraceSELECTTM for trace analysis >69 %) and heated at the boiling point for 2 h to decompose the organic components. Afterwards, the solution was diluted to a final volume of 25 mL with ultrapure water (18.2 MΩ·cm, PureLab Pro, ELGA LabWater, High Wycombe, Bucks, UK) for analysis by ICP-OES. Phosphorus levels were measured using an Optima 8000 ICP-OES (Perkin Elmer, Waltham, MA, USA), operated at 1500 W and equipped with an autosampler S10, MiraMist® nebulizer, and a cyclonic chamber. Argon (420.069 nm) was used as the internal standard. Calibration was performed using commercial standard solutions (Fluka TraceCERT©), diluted in 2 % HNO_3. Phosphorus emission was monitored at a wavelength of 213.617 nm.

2.3.13. Photoactivity tests

Standard irradiation experiments were conducted by mixing 1.5 mL of DPBF in ethanol solution with 1.5 mL of the 2D-bP suspension. Since DPBF in a water/ethanol (50:50) mixture shows a 50 % sensitivity for singlet oxygen ($^1O_2$) species [30], a 1:2 concentration ratio between 2D-bP and DPBF was adopted to minimize the formation of $^1O_2$ molecules that would not interact with the trap. Therefore, the concentrations of DPBF and 2D-bP were adjusted to maintain a 2:1 wt ratio (DPBF:2D-bP). The Xenon lamp of the FluoroMax-4 was used as the irradiation source, and the excitation spectrum was recorded (experimental settings: excitation range of 650–1150 nm, 20 nm slit). The production of $^1O_2$ was confirmed through UV-Vis measurements by observing the decrease in absorption of DPBF at 410 nm.

2.3.14. Thermal degradation test

Two distinct experiments were designed to investigate the thermal degradation of 2D-bP/PLGA composite materials. In the first experiment, low-temperature thermal degradation was examined: 10 mg of the samples were placed in an oven at 60°C for various durations: 6, 21, 27, and 40 h. After heating, the samples were removed from the oven and stored in a refrigerator until they were analyzed using SEC to assess changes in molecular weight. In the second experiment, high-temperature thermal degradation was examined: 10 mg of the samples were placed in the oven for 40 h at different temperatures (60, 90, 150, and 200°C). Upon removal from the oven, the samples were stored in a refrigerator and were analyzed using SEC to assess changes in molecular weight.

2.3.15. Hydrolytic degradation tests

The hydrolytic degradation of 2D-bP/PLGA samples was examined by suspending 10 mg of the samples in 2 mL of water at 40°C. The samples were maintained in water for various time intervals (1, 3, 7, and 10 days), after which they were refrigerated and freeze-dried prior to SEC analysis to assess any changes in molecular weight.

3. Results and discussion

3.1. Preparation and characterization of 2D-bP suspensions

BP crystals were exfoliated by ultrasonication in a de-aerated water solution of SDS (1 wt%), followed by subsequent centrifugation at increasing rotation speeds to isolate 2D-bP with reduced dimensions. The resulting nanoflakes were thoroughly characterized via DLS, Raman, UV-Vis, XPS, AFM, SEM, and TEM (Fig. 1 and Figure ESI 2).

Our findings are consistent with those reported by Hersam [19], although we used a reduced SDS concentration (1 % wt/vol). Visual inspection of the suspensions, pre- and post-centrifugation, revealed a color shift from dark brown to pale yellow (Figure ESI 2 A), indicating sedimentation of thicker flakes. DLS analysis showed that increasing the centrifugation speed from 3000 to 14,000 rpm reduced particle size from ~110 nm to ~10 nm, with narrower distributions (Figure ESI 2B). A control exfoliation in pure deoxygenated water (no SDS) yielded slightly larger flakes after centrifugation at 7000 rpm (Figure ESI 2B, green curve), thus confirming the beneficial effect of the surfactant (SDS). UV-Vis spectra (Figure ESI 2 C) of 2D-bP suspensions exhibited a profile like those found in the literature [32,33] including a broad absorption band below 600 nm likely arising from the combined contributions of high-energy transitions influenced by flakes size [14,19,33]. A noticeable increase in the baseline, particularly for samples containing larger particles, was attributed to a scattering effect. Absorbance values at 466 nm were corrected by subtracting absorbance at 900 nm (as in [14]), and the Lambert–Beer law was applied to estimate 2D-bP concentration using extinction coefficients determined via ICP-OES (Table ESI 1). Results confirmed higher 2D-bP concentrations in SDS suspensions, underlining the surfactant's role in enhancing exfoliation yield and dispersion stability. Raman spectroscopy (Figure ESI 2D) confirmed the crystalline structure of exfoliated bP. The characteristic vibrational modes: A_g^1 (~362 cm^{-1}), B_{2g} (~438 cm^{-1}), and A_g^2 (~465 cm^{-1}) were detected in both exfoliated 2D-bP (centrifuged at 7000 rpm) and bulk bP. While exfoliation-induced shifts to higher wavenumbers, particularly for the A_g^2 mode [29,34] [35,36], are

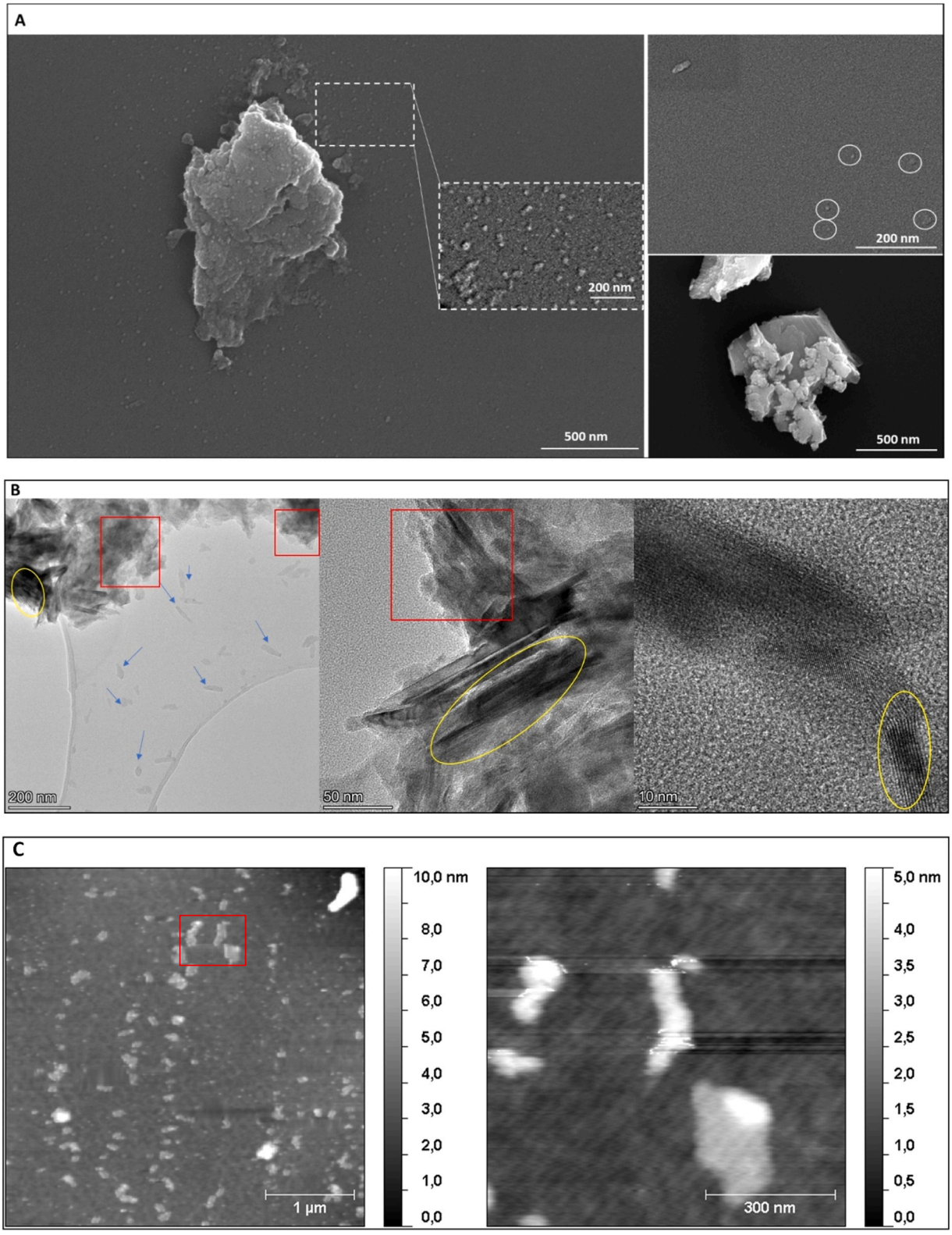

Fig. 1. A: SEM images of a 2D-bP suspension (supernatant of centrifugation at 7000 rpm) and spin-coated on a silica wafer: (left) bigger aggregate surrounded by smaller flakes, (right) small flakes homogeneously dispersed, and coarser aggregate. B: TEM images of 2D-bP flakes, precipitated at 14,000 rpm from the supernatant of centrifugation at 7000 rpm: the sample contains both well-dispersed (blue arrows) and aggregated flakes (red square), but also non-exfoliated bulk bP (yellow circles). C: AFM image of the same 2D-bP flakes suspension spin-coated on a silica wafer; (right) zoom in the region marked with a red square.

minimal (2–3 cm^{-1}) and limited to monolayer and bilayer bP, a more informative trend emerges from the analysis of peaks intensity. Indeed, we observed that the intensity difference between A_g^2 and $B_{2\,g}$ peaks increased from 27 for bulk bP to 64 for 2D-bP, and the integrated ratio of A_g^2 to A_g^1 peaks rose from 1.26 for bulk bP to 1.86 for 2D-bP. These values are in alignment with the literature [35,36] suggesting that the 2D-bP flakes consist of few-layer structures ($\geq$ 6 layers), as expected for liquid phase exfoliation [19].

The SEM measurement revealed flakes with a wide range of dimensions, from about 50–100 nm to 1–2 μm. As shown in Fig. 1A, a relatively large and not-well-exfoliated flake (500 nm) is visible surrounded by smaller 2D-bP flakes with dimensions consistent with the DLS data (50–80 nm). On the right of the figure smaller flakes appear homogeneously dispersed alongside coarser aggregates. The flakes size observed is in agreement with the average values from DLS measurement. While SEM also detected larger, poorly exfoliated aggregates that were not captured in the scattering analysis, it is worth noting that DLS measurements provide a number-averaged estimation reflecting primarily the lateral dimensions of similarly sized flakes. These flakes represent the predominant population observed in the SEM images.

TEM analysis further confirmed the presence of very small 2D-bP flakes, with dimensions consistent with those observed in SEM and DLS measurements (indicated by blue arrows). The sample preparation method has led to partial re-aggregation of the flakes in an anisotropic manner (highlighted by red squares), likely due to the local concentration effect. Additionally, distinct areas of the sample containing non-exfoliated bP can be clearly identified (marked with yellow circles). The AFM analysis provided further insights into the dimensions and distribution of the flakes. The height measurements range from 3.5 to 5 nm (Fig. 1C), which matches the data reported in the literature for 2D black phosphorus prepared through liquid-phase exfoliation [37]. This evidence confirms that, realistically, the flakes are composed of a few layers. By taking into account that single-layer phosphorene has a thickness of about 0.9 nm [38], the exfoliation gives three to six layers of 2D-bP flakes, as also demonstrated by Raman.

A notable feature observed in the AFM images is the presence of white, unstable regions on the upper surface of many flakes, which may be attributed to SDS residues decorating the 2D-bP surface. Although the surfactant interacts with the flake's surface through secondary interactions, these interactions can be disrupted by the probe during measurement leading to instability zones, affecting the quality of the final image. The covering effect of SDS is further confirmed by XPS analysis (Figure ESI 3). Although the phosphorus signals were very weak and close to the background noise, distinct signals of carbon and sulfur attributable to SDS were clearly detected. An oxygen signal was also observed, which also comes from the silicon substrate. These findings suggest that SDS is adsorbed on the surface of the flakes, forming a protective layer over the underlying phosphorus. While SDS effectively stabilizes the flakes, it also obscures the phosphorus signal during XPS analysis. This observation is in agreement with the AFM measurements and supports the hypothesis that SDS acts as decorating and stabilizing agent on the 2D-bP nanoparticles.

3.2. Water stability of 2D-bP suspensions

As extensively reported in the literature, the major drawback of bP and its exfoliated species is the instability in air and humidity [39,40] owing to noticeable reactivity with oxygen. This is strictly related to 2D-bP chemical structure: each phosphorus atom is covalently bound to three other atoms and has a dangling lone pair pointing out of the layer's plane, which makes 2D-bP highly susceptible to oxygen, leading to oxidative degradation. Since oxygen is quite soluble in water (8 mg/L), an initial degradation may occur during the exfoliation process, when the P-P secondary bonds between layers of bulk bP are broken to form single and few-layer flakes. These flakes present a higher available surface area, which increases the exposure of dangling bonds to the possible interaction with oxygen molecules, thus increasing the degradation probability and rate. Theoretical studies suggest that water does not interact with the pristine 2D-bP surface, which explains its limited ability to stabilize nanoparticles by solvation, but after the surface oxidation, the interaction becomes favourable. Indeed, water can remove P_xO_y species from the nanoflakes' surface, exposing P^0 to continue oxidation [39]. This supports the experimental results of a faster degradation rate of 2D-bP suspended in water [14]. To evaluate the possible stabilizing effect of surfactant, we monitored the temporal stability of 2D-bP suspensions exfoliated in water alone and with SDS (Fig. 2). The two suspensions (water-only and water-SDS) were prepared using the same procedure, with the only difference being the surfactant's presence.

Degradation was assessed from the decrease in absorbance of the suspensions, always considering 466 nm as the reference wavelength (Figure ESI 4). The results clearly show that the SDS-stabilized 2D-bP suspension exhibits greater long-term stability than the suspension in pure water. As shown in Fig. 2, the normalized absorbance at 466 nm decreases much more slowly in the presence of SDS: after three days, the absorbance of the SDS-containing suspension drops by only a ~20 %, whereas that of the water-only suspension drops by ~30 % after two days and ~50 % after four days. Following this initial phase, both suspensions continue to degrade, with absorbance values approaching zero by day 11 for the water-only sample and around day 20 for the SDS-stabilized one. Therefore, the presence of the surfactant plays a significant role, not just in increasing exfoliation yields (see Table ESI 1), but also in stabilizing the 2D-bP flakes. The assessed decoration effect may also have a fruitful role in partially shielding 2D-bP flakes' surface from the interaction with dissolved oxygen, thus slowing down the oxidative degradation process.

As previously discussed, the progressive decrease in absorbance intensity is attributed to the oxidative degradation of 2D-bP flakes leading to soluble P_xO_y species formation. This process is confirmed by the FTIR-ATR analysis of fresh and aged (14-day-old) precipitates obtained from centrifuged 2D-bP water-SDS suspensions (Figure ESI 5 A). In the aged sample, distinct peaks appear in the 900–1200 cm^{-1} region, corresponding to P-O stretching vibration [41], which are indicative of oxidized phosphorus species. Even though it is not easy to accurately attribute the peaks due to the vibrational contribution of the P-O bonds, it can be deduced that there is a slight oxidation also in the fresh sample, which seems, however, different from that of the aged sample. Additional confirmation comes from XPS analysis (Figure ESI 5B). Although, as discussed above, the phosphorus signal is very weak, it was

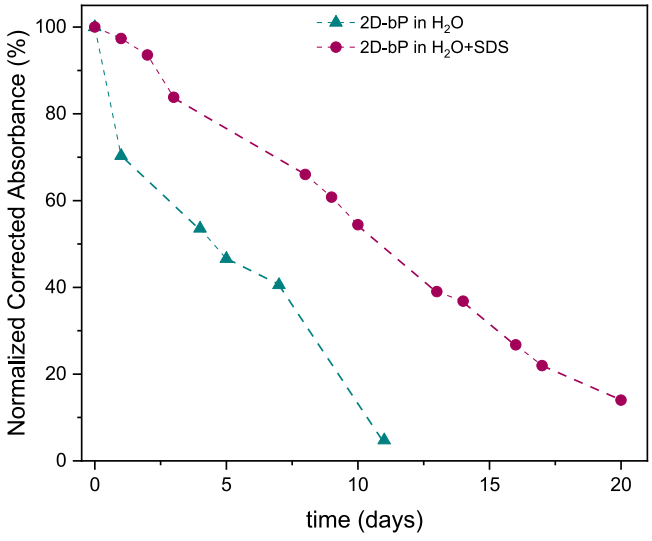

Fig. 2. Normalized and corrected absorbance (A_{466}-A_{900}) of 2D-bP exfoliated in water and water and SDS.

nevertheless possible to carry out a deconvolution of the peaks for both fresh and aged samples. The aged sample shows a decrease in the intensity of the P^0 signal ($2p_{3/2}$ and $2p_{1/2}$), accompanied by a notable increase in peaks at higher binding energies corresponding to oxidized forms of phosphorus [42].

3.3. Preparation and characterization of bP/PLGA nanocomposites

PLGA, a biodegradable and biocompatible polymer, has been used to encapsulate, protect, and stabilize 2D-bP, aiming to develop new nanomaterials for biomedical applications with particular reference to photothermal therapy [28]. Given the limited insights available in the literature on these innovative systems, we have prepared, studied, and characterized nanocomposites based on PLGA and 2D-bP to better understand their physical-chemical characteristics and application possibilities. The main purpose was to investigate the interfacial interactions between PLGA and 2D-bP nanoflakes and to evaluate the impact of these nanoflakes on the degradation processes that naturally occur during applications. In addition, it is necessary to prove that the nanoflakes remain photoactive and/or effective for drug delivery or PDT applications. Nanocomposite films were prepared using the procedure reported in Figure ESI 1, thus allowing the production of PLGA-based materials with varying filler sizes and concentrations. Indeed, three nanocomposites were prepared whose composition and flake dimensions are reported in Table 1.

PLGA+bP_1 has the lowest values of size and concentration of bP nanoflakes as derived from a centrifugation speed of 7000 rpm. Instead, PLGA+bP_2 is obtained by exfoliating the unexfoliated bP precipitated at 7000 rpm, then centrifuging it at 3000 rpm to separate flakes from the liquid medium. BP flakes obtained from this fraction are bigger than the previous ones. Finally, PLGA+bP_3 is obtained by adding all the residual bP precipitated at 3000 rpm to the PLGA matrix (see Figure ESI 1).

Nanocomposite films were first characterized through FTIR and Raman spectroscopies. PLGA shows the characteristic IR spectrum of PLA copolymers (Fig. 3). In the region between 3450–3500 cm^{-1} there are the absorptions associated with the stretching of terminal -OH groups. Peaks in the range of 2885–3010 cm^{-1} correspond to C–H stretching related to the polymer backbone, while the characteristic C═O stretching peak appears at 1756 cm^{-1} . Additionally, the spectrum includes C–H bending vibrations (1450–850 cm^{-1}), C–O stretching vibrations (1186–1089 cm^{-1}), and the fingerprint region at lower energies.

The two monomers composing the PLGA, lactic acid and glycolic acid, differ in their substitution at the α-position of the carbonyl group (-CH_2- for glycolic acid and -$CH(CH_3)$- for lactic acid). By comparing the spectrum of PLGA with those of the two homopolymers, poly(lactic acid) (PLA) and poly(glycolic acid) (PGA), it is possible to assign the peaks in the C–H bending region to their respective monomeric units [43]. The 1454 and 1394 cm^{-1} peaks are attributed to the units deriving from lactic acid and correspond to the bending of CH_3 and CH, respectively [44]. The peak at 1424 cm^{-1} is instead due to the glycolic units and corresponds to the CH_2 bending [45]. The IR spectra of the composites

Table 1
Characteristics of nanocomposites.

code	2D-bP concentration (%wt)[a]	2D-bP size (nm)[b]
PLGA+bP_1	~0.05	~ 50
PLGA+bP_2	~0.1	~100
PLGA+bP_3	~4	-[c]

[a] The concentration of the 2D-bP in the composites was determined by using the corrected absorbance values at 466 nm of 2D-bP suspensions used (for the PLGA+bP_1 and PLGA+bP_2 samples). For the PLGA+bP_3 sample, the concentration was estimated by calculating the difference relative to the initial amount of bulk bP.

[b] DLS measurement of 2D-bP suspensions.

[c] Not determined

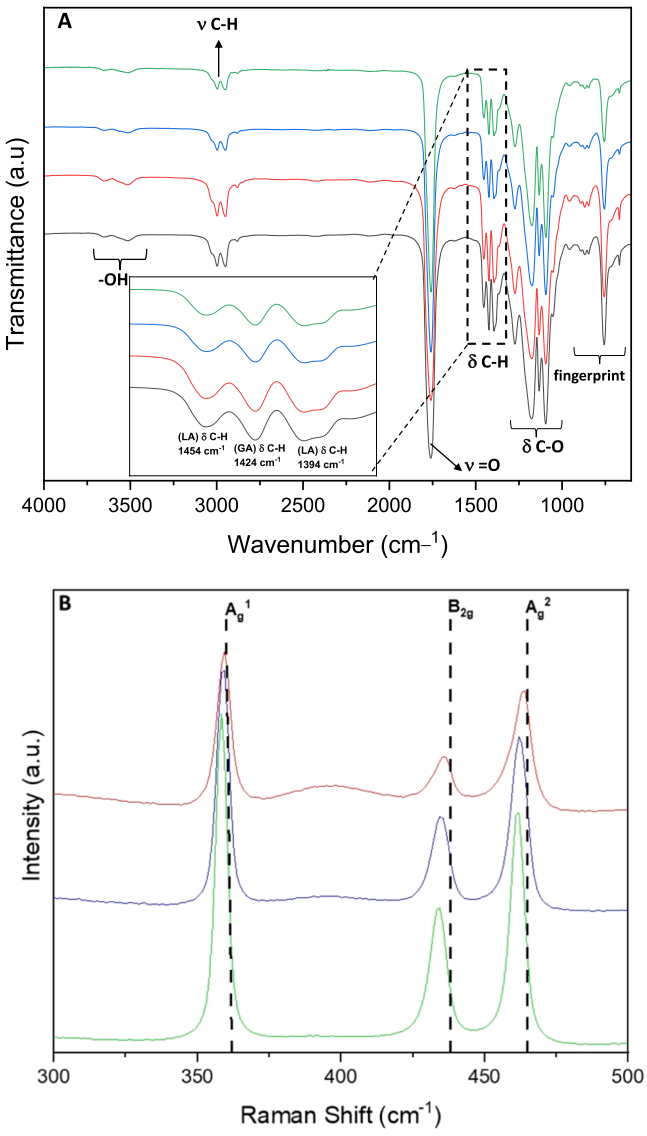

Fig. 3. A: FTIR spectra of PLGA (black), PLGA+bP_1 (red), PLGA+bP_2 (blue) and PLGA+bP_3 (green) samples. B: Raman spectra of PLGA+bP_1 (red), PLGA+bP_2 (blue) and PLGA+bP_3 (green) samples. (λ=785 nm); the dashed black lines represent Raman peaks for 2D-bP from the water and SDS suspension (A_g^1=362 cm^{-1}, $B_{2\,g}$ =438 cm^{-1}, and A_g^2 =465 cm^{-1}).

are perfectly superimposable with that of the original copolymer, suggesting that bP does not appreciably alter the characteristic absorptions of the polymer matrix. At the same time, no characteristic signals of P_xO_y species in the 1060–1160 cm^{-1} range are observed, suggesting a low level of oxidation in the flakes.

Raman spectra (Fig. 3) of the three nanocomposites show the characteristic Raman peaks of bP attributable to the vibrational modes A_g^1 (~362 cm^{-1}), $B_{2\,g}$ (~438 cm^{-1}), and A_g^2 (~465 cm^{-1}). As we can observe, the typical 2D-bP Raman peaks for composites are red-shifted toward lower energies, with respect to the ones of 2D-bP exfoliated in water and SDS (Fig. 3B, dashed black lines). This could be explained by considering the presence of the polymer, which surrounds and encapsulates flakes, reducing vibrational freedom and lowering the energy associated with each mode. Furthermore, it can be observed that samples PLGA+bP_2 and PLGA+bP_3, with higher concentrations of flakes and broader size distributions (including residual bulk bP in sample_3), show a slightly greater red-shifted Raman peaks than those of the PLGA+bP_1 sample, which instead has a higher degree of flakes exfoliation. This suggests that the highly viscous polymer matrix in

PLGA+bP_1 prevents flake migration and re-aggregation during dispersion, maintaining a better exfoliation state. Analyzing solid samples highlights these differences in exfoliation, with the red shift correlating with flake thickness (few-layer flakes in PLGA+bP_1 versus bulk bP in PLGA+bP_3). Micro Raman analysis also provided insights into nanocomposites at the microscopic level (Figure ESI 6 A). In the PLGA+bP_1 and PLGA+bP_2 samples from the flakes measure between 60 and 100 nm, too small to be visible with the microscope used in the Raman analysis. These two samples also contain a few larger non-exfoliated particles that are unevenly dispersed throughout the nanocomposite. In contrast, the PLGA+bP_3 sample prepared from the precipitate obtained at 3000 rpm, contains a broader distribution of larger, powdery bP aggregates, including both 2D and bulk bP. Raman spectra were acquired in zones of the samples free of coarse aggregates, confirming the presence of small 2D-bP flakes well dispersed in all the samples. These morphological features were also supported by SEM and EDS analysis (Figure ESI 6B). Samples PLGA+bP_2 and PLGA+bP_3 (the only analyzed composites since PLGA+bP_1 has a 2D-bP concentration which falls below the EDS detection limit) appear relatively homogeneous, even if some bigger micrometric aggregates are present. EDS further confirmed the presence of phosphorus.

The DSC measurement of the blank sample evidenced a glass transition temperature (Tg) of 47.4 ± 0.1°C, in agreement with both experimental and theoretical data from the literature for the 50:50 copolymer [46,47]. The presence of 2D-bP does not seem to significantly affect the Tg of the polymer in the PLGA+bP_1 (47.4 ± 0.2°C) and PLGA+bP_2 (47.3 ± 0.1°C) samples, which contain lower filler concentrations with smaller average flake dimensions. In contrast, PLGA+bP_3 presents a slightly higher Tg value (48.2 ± 0.1°C) (Fig. 4A). This result can be rationalized considering the higher filler concentration of the PLGA+bP_3 sample (~4 wt%), constituted by a powdery mixture of unexfoliated bulky bP and bigger 2D-bP flakes. Thus, the Tg increase can be explained by a classical *filler effect* due to the presence of the bP, whose interactions with polymer chains at the interface cause a decrease in macromolecules' mobility [48].

TGA (Fig. 4B and Table ESI 2) showed that the incorporation of 2D-bP improves the thermal stability of the nanocomposites compared to neat PLGA. This is evidenced by the shift of both, T_{onset}, and T_{infl} to higher temperatures, indicating delayed thermal degradation. Under the rapid heating conditions of TGA and nitrogen atmosphere, degradation mainly occurs by cracking [48], breaking polymer chains into volatile fragments. The stabilizing effect of 2D-bP can be attributed to two main factors: firstly bP is a good thermal conductor [49] that absorbs heat supplied to the sample during the analysis, reducing local temperature around the flakes and delaying the degradation of the polymer; secondly, the layered structure of 2D-bP can act as a physical barrier, hindering the diffusion of volatile degradation products.

Considering the thermal behaviour of the different samples (Table ESI 2) two aspects must be considered: 2D-bP content and surface-to-volume ratio. The most stable sample, PLGA+bP_1, contains the lowest bP content but has the best exfoliation, leading to a larger interfacial area with the polymer. This enhances heat dissipation and delays degradation more effectively than samples with higher but less delaminated bP content (e.g., PLGA+bP_3). The results suggest that filler morphology and dispersion play a key role, sometimes more critical than the absolute concentration [50].

Two additional degradation tests (thermal and hydrolytic) were then designed to better understand the nature of the stabilizing effect observed by TGA analysis and investigate the degradative behaviour of composite materials.

Samples were maintained at 60, 90, 150, and 200 °C for 40 h in an oven and analyzed by SEC to evaluate the variation of PLGA molecular weights (Fig. 5 and Table ESI 3). The first temperature (60°C) is over the glass transition temperature of PLGA (48°C), and it is also the reference temperature for biopolymer degradation in industrial compost plants [51]; 200 °C is below the onset of PLGA degradation, determined by TGA. Fig. 5 reports the decrease in $\overline{M_n}$and $\overline{M_w}$obtained from the SEC measurement after the degradation test.

As expected, an increase in temperature leads to a decrease in molecular weights. However, the reduction observed at 60°C is minimal: after 40 h, the samples exhibit an average weight loss of approximately 8 % relative to their initial weight. This limited degradation is likely due to the low temperature, which, although above the Tg, is insufficient to trigger significant polymer chain breakdown.

It has been reported that, at low temperatures, PLGA, like PLA and PGA, undergo degradation primarily via backbiting [52]. This mechanism involves intramolecular transesterification initiated by a terminal hydroxyl group, leading to the formation of cyclic dimers. These further degrade into monomers and ultimately into CO_2 and water through decarboxylation. SEC analysis also shows that the presence of 2D-bP slightly accelerates degradation in PLGA+bP_1 sample, which features smaller and better-exfoliated 2D-bP flakes. This observation contrasts with previous TGA results, where 2D-bP was found to enhance the thermal stability of composites. This apparent inconsistency likely arises from the different degradation conditions: TGA is performed at high temperatures under inert atmosphere, while the thermal degradation

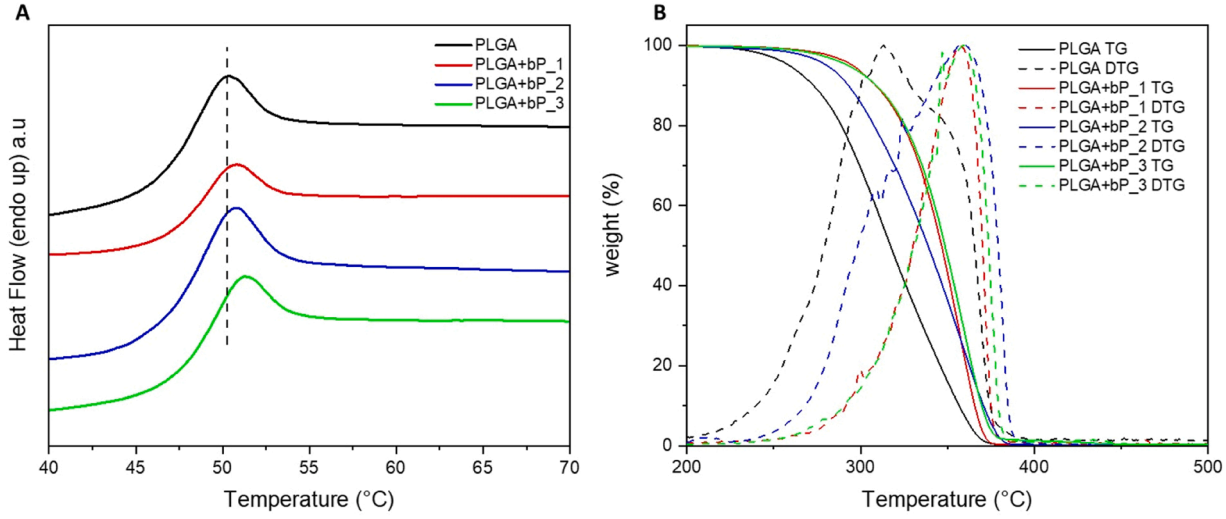

Fig. 4. A: DSC curves (second heating) and B: TGA (straight line) and DTG (dashed lines) patterns for neat PLGA and PLGA+bP samples. (All the measurements were repeated 3 times for each sample).

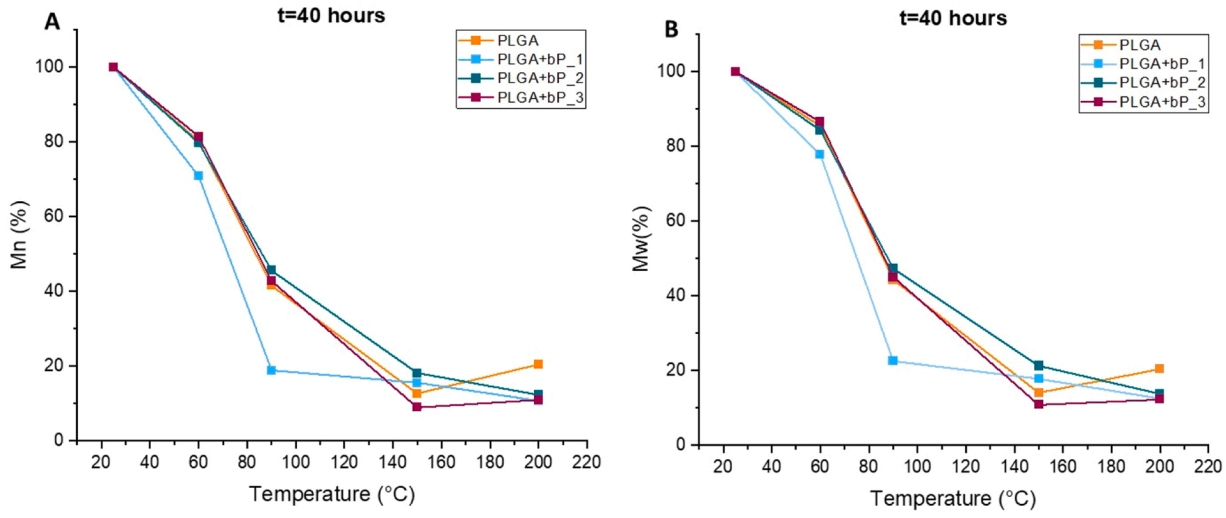

Fig. 5. Normalized $\overline{M_n}$ (A) and $\overline{M_w}$(B) after degradation tests at 60, 90, 150 and 200°C.

studied here occurs at lower temperatures in the presence of oxygen. Under these conditions, the finely exfoliated 2D-bP flakes in PLGA+bP_1 may promote enhanced interfacial interactions with the polymer matrix, potentially affecting the degradation behavior. Specifically, the lone pairs on the 2D-bP can interact with the terminal carbonyl groups of PLGA, inducing polarization of the bond and thereby facilitating the backbiting process, which influences the degradation mechanism. However, a direct catalytic role of 2D-bP in low-temperature degradation cannot be confirmed.

To investigate the impact of thermal degradation on the polymer's structural characteristics, FTIR analysis was performed on the samples before and after 40 h of thermal exposure at 150 °C (Figure ESI 7). The results showed no significant structural changes related to the presence of 2D-bP, indicating that the filler does not substantially affect the polymer's vibrational profile even after prolonged heating

Recognizing that understanding polymer degradation is crucial for optimizing the performance of biodegradable polymers in biomedical applications, a hydrolytic degradation test was designed to investigate whether the interactions between 2D-bP and PLGA could influence the degradation process that the biopolymer undergoes in aqueous environments [53]. Nanocomposite samples were suspended in water, kept at 40°C for different times (1, 3, 7, and 10 days), and analyzed by SEC. PLGA is known to degrade via hydrolysis of ester bonds in its backbone, a process autocatalyzed by carboxylic end groups and leading to oligomers, soluble monomers, and eventually CO_2 and water [24]. The degradation rate depends on several parameters, including molecular weights, stereochemistry, end-group functionalization, and LA/GA ratios. By increasing the amount of LA, the copolymer is more hydrophobic, more crystalline and more resistant to degradation. However, PLGA 50:50 amorphous copolymers, such as the one used in this work, exhibit measurable degradation. SEC analysis (Fig. 6, Table ESI 4) revealed a marked decrease in molecular weights of all samples reaching approximately 98 % after 10 days. The presence of bP does not significantly affect the polymer degradation, and all the curves overlap.

To further investigate the effects of hydrolytic degradation, IR analysis was performed on the residues after 10 days of incubation in water at 40°C and compared to the spectrum of the pristine samples. Significant changes were observed. In particular, an increase in the OH absorption band indicated the formation of hydroxyl-containing degradation products (Figure ESI 8 A). Changes were also detected in the CH bending region, reflecting structural alterations in the polymer backbone. In the fingerprint region (1500–1300 cm^{-1}, Figure ESI 8B) normalization to the characteristic signal of CH_3 at 1453 cm^{-1} (LA units) revealed a significant reduction in the intensity of the peak at 1424 cm^{-1} relative to the CH_2 groups (GA units). It is indeed reported that glycolide units are more hydrophilic, and the hydrolysis of ester

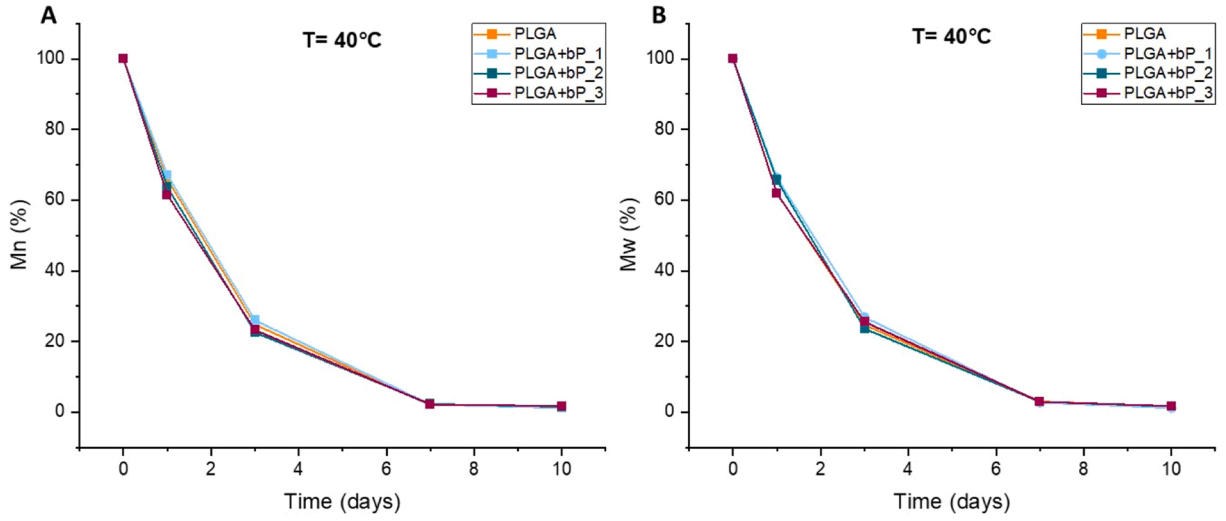

Fig. 6. Normalized $\overline{M_n}$(A) and $\overline{M_w}$(B) following hydrolytic degradation test.

bonds between two glycolide units occurs at a faster rate [54,55]. The reduction of this signal confirms the preferential loss of glycolic acid units during degradation. Importantly, no significant spectral differences between the nanocomposites and the neat polymer were evidenced, indicating the presence of bP does not alter the chemical structure of the degradation products.

Even though the hydrolytic degradation was conducted in an aqueous solution at 40°C under ambient conditions, i.e., without any protection from contact with air, Raman spectra of the dried nanocomposite residues after 10 days still show characteristic 2D-bP signals

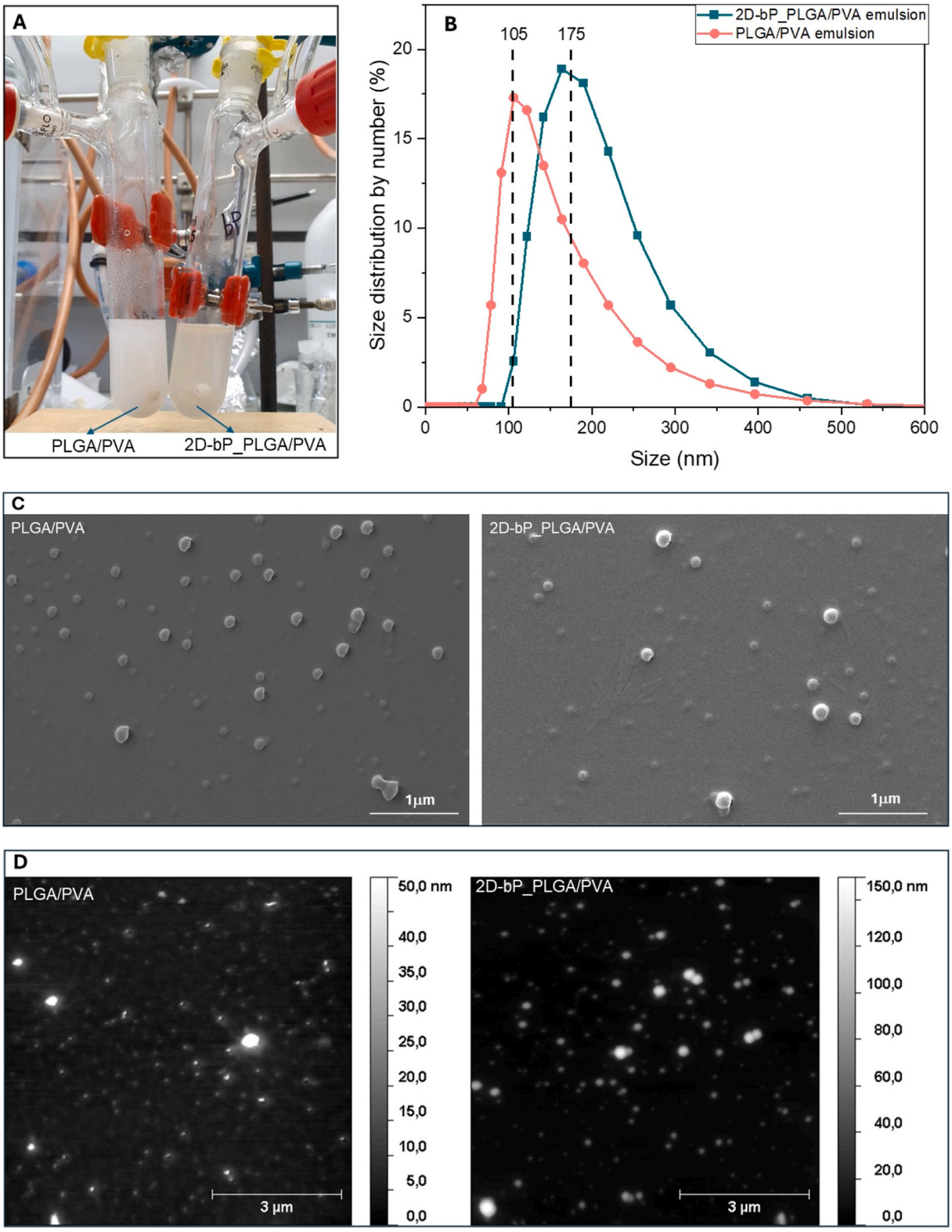

Fig. 7. A: Picture of PLGA/PVA and 2D-bP_PLGA/PVA emulsions; B: Size distribution of micelles obtained by DLS; C: SEM and D: AFM images of 2D-bP_PLGA/PVA and blank PLGA/PVA emulsions.

(Figure ESI 8 C). This demonstrates that, despite the favourable conditions for oxidative degradation of bP, especially when it is exfoliated in the samples PLGA+bP_1 and PLGA+bP_2, its encapsulation within the polymer matrix effectively preserves the nanoflake structure, even as the surrounding polymer undergoes substantial degradation.

3.4. Preparation and characterization of bP/PLGA emulsions

Classical nanocomposites based on 2D-bP and PLGA, obtained by solvent casting, are not suitable for evaluating properties more directly related to biomedical applications, such as photoactivity.

Emulsions of 2D-bP in PLGA were prepared using the well-established oil-in-water method [28] to evaluate their possible biomedical applications and protect 2D-bP from oxidation. Micelles were prepared operating above the critical micellar concentration (CMC) of PLGA (0.31 mg/mL) [56] and in the presence of PVA as surfactant/emulsifier, whose concentration also plays a significant role in driving the formation of polymer micelles [57]. In our experimental conditions, the PVA concentration was set below its critical aggregation concentration (CAC= 9.2 mg/mL) to prevent the formation of aggregates and promote the formation of PLGA particles. We also prepared a blank emulsion with only PLGA and PVA for comparison (Fig. 7A). Emulsions were first characterized through DLS to gain insight into the dimensions of micelles and evaluate whether the presence of 2D-bP could affect them (Fig. 7B). As it is possible to observe, the blank sample has smaller average dimensions (~105 nm) than 2D-bP_PLGA/PVA (~175 nm), suggesting the effective embedding of the 2D-bP flakes in the core of micelles. Furthermore, the difference between the mean values of emulsion's size distributions with and without 2D-bP (~70 nm) is approximately equal to the mean particle size of 2D-bP flakes (50–70 nm), measured by DLS analysis (Figure ESI 2B). SEM images reported in Fig. 7C show the presence of spherical particles in both samples, with micelles having dimensions of about 100–200 nm with broader distribution; the particle's morphology and size shown in the images, although representative of only a small area of the sample, can be considered in quite good agreement with the DLS data. AFM measurement (Fig. 7D) shows that the average dimensions of particles agree with SEM and DLS data. However, it can be partially distinguished between the emulsion with and without 2D-bP; indeed, micelles from the blank sample appear smaller than the ones with 2D-bP. The lateral height also varies significantly between the samples. For the emulsion without 2D-bP, a maximum abscissa value of 50 nm was set to enhance image contrast. Instead, for the emulsion containing 2D-bP, the average particle size was larger, necessitating a maximum abscissa value of 150 nm to accommodate the increased dimensions.

Although these images capture only specific areas of the samples and a varied distribution of dimensions is still observed, it can be concluded that the micelles in the blank emulsion are smaller than those in the emulsion containing 2D-bP. This observation supports the hypothesis that embedding the 2D-bP flakes within the micelles causes their volumetric enlargement.

It is also worth noting that lateral dimensions are slightly smaller than the particle diameters, which could be attributed to a flattening effect induced by the spin-coating procedure used to prepare the samples.

3.5. Photoactivity of 2D-bP samples

As previously mentioned, 2D-bP exhibits photosensitising properties, generating $^1O_2$ species upon interaction with appropriate wavelengths. In particular, for both excited singlet species, the $^3O_2/^1O_2$ redox potentials (1.6 eV for $^1\Sigma^+_g$ and 0.98 eV for Δ_g) fall between the band gap of 2D-bP (0.3–2 eV), perfectly fitting the needs for $^1O_2$ formation. However, increasing the number of layers up to bulk bP, the bandgap drops below the redox potential, limiting $^1O_2$ generation [29]. The photogeneration ability, combined with its biocompatibility, makes 2D-bP especially suitable for PDT applications [58].

To test the ability of 2D-bP water suspension and 2D-bP_PLGA/PVA emulsion to produce $^1O_2$, we use DPBF as a probe molecule. DPBF can react with $^1O_2$, undergoing a Diels-Alder 1,4-cycloaddition; this reaction causes a decrease in the absorbance of DPBF at 410 nm, allowing the control of the $^1O_2$ production over time [14,30].

The optimal wavelength range for activating a photosensitizer is between 600 and 800 nm. This range is referred to as the "optimal therapeutic window" because it includes wavelengths that are therapeutically safe while providing enough energy to facilitate the transition of oxygen to its excited singlet state without causing damage to biological tissues [59]. When suspensions of 2D-bP are irradiated with light in this range, light is absorbed by phosphorus atoms composing the flakes. This energy is then transferred to oxygen molecules, producing $^1O_2$ species, which can react with DPBF through a Diels-Alder cycloaddition, causing a reduction in its absorbance intensity at 410 nm.

First, we evaluated the stability of DPBF upon irradiation, and no significant reduction of the trapper absorbance (Fig. 8A) was observed after 5 irradiation cycles (see experimental part).

Conversely, during the irradiation of the sample 2D-bP (Fig. 8B), the absorbance at 410 nm significantly decreased from 0.99 to 0.45, confirming the photoactivity of the flakes and their ability to generate $^1O_2$ [14,60]. Since the excitation frequencies are characteristic of the visible and near-infrared regions, we tested another aliquot of the suspension with DPBF by placing the cuvette in sunlight and recording the UV-Vis spectrum at intervals consistent with the previously mentioned irradiance cycles. A decrease in absorbance at 410 nm, approximately 10 %, was observed (see Figure ESI 9), indicating that 2D-bP is photoactive even when exposed to solar radiation [61]. However, irradiation under controlled conditions is more effective in generating $^1O_2$, resulting in an absorbance decrease of 55 %.

When dissolved in water/ethanol (50:50), DPBF has a sensitivity of 50 % for $^1O_2$ species [30]. Based on this consideration, we tried to estimate quantitatively the amount of $^1O_2$ produced by 2D-bP flakes (Table 2).

From data in Table 2, it can be observed that the amount of DPBF moles reacting and, therefore, the amount of $^1O_2$ moles produced are quite steady (with the exception of the final cycle, due to unavoidable variability) [14], confirming the photocatalytic activity of 2D-bP in the production of $^1O_2$. The total amount of $^1O_2$ produced over the irradiation experiment is calculated as the sum of singlet oxygen moles produced in each cycle, and it is equal to 14.04×10^{-8} mol, which corresponds to $\sim 2.2 \times 10^{-3}$ mg (MW(O_2) = 16 g/mol). This quantity has been produced from a starting amount of 2D-bP of 0.015 mg. Based on our measurements, 2D-bP exfoliated in water and SDS has a high generation efficiency of $^1O_2$. Considering the safety and biocompatibility of the exfoliation medium, this system holds significant potential as an effective platform for PDT.

Polymeric embedding has been widely proposed to enhance the stability of 2D-bP, including in biomedical applications [28,62]. Therefore, it is important to investigate the photosensitizing properties of 2D-bP_PLGA/PVA emulsion. By employing the same irradiation conditions previously described, the photoactivity of emulsion samples was tested. Fig. 8C shows that the absorbance decrease at 410 nm is significantly lower (~3 %) than that of the 2D-bP suspension, suggesting a lower production of $^1O_2$. Indeed, the encapsulation of 2D-bP in PLGA micelles seemed to cause significant insulation of nanoflakes from oxygen, probably due to PLGA hydrophobicity and its barrier properties to oxygen. It is known that PLGA copolymer films, with at least 50 % glycolide content, present barrier properties to oxygen and water that are comparable to those of poly(ethylene terephthalate) (PET) [63]. Thus, the encapsulation of 2D-bP into polymer micelles prevents them from interacting with oxygen, highly reducing the photosensitizing activity, even upon irradiation.

The photoactivity reduction of the emulsion confirms our hypothesis on the system's morphology; realistically, flakes are located inside

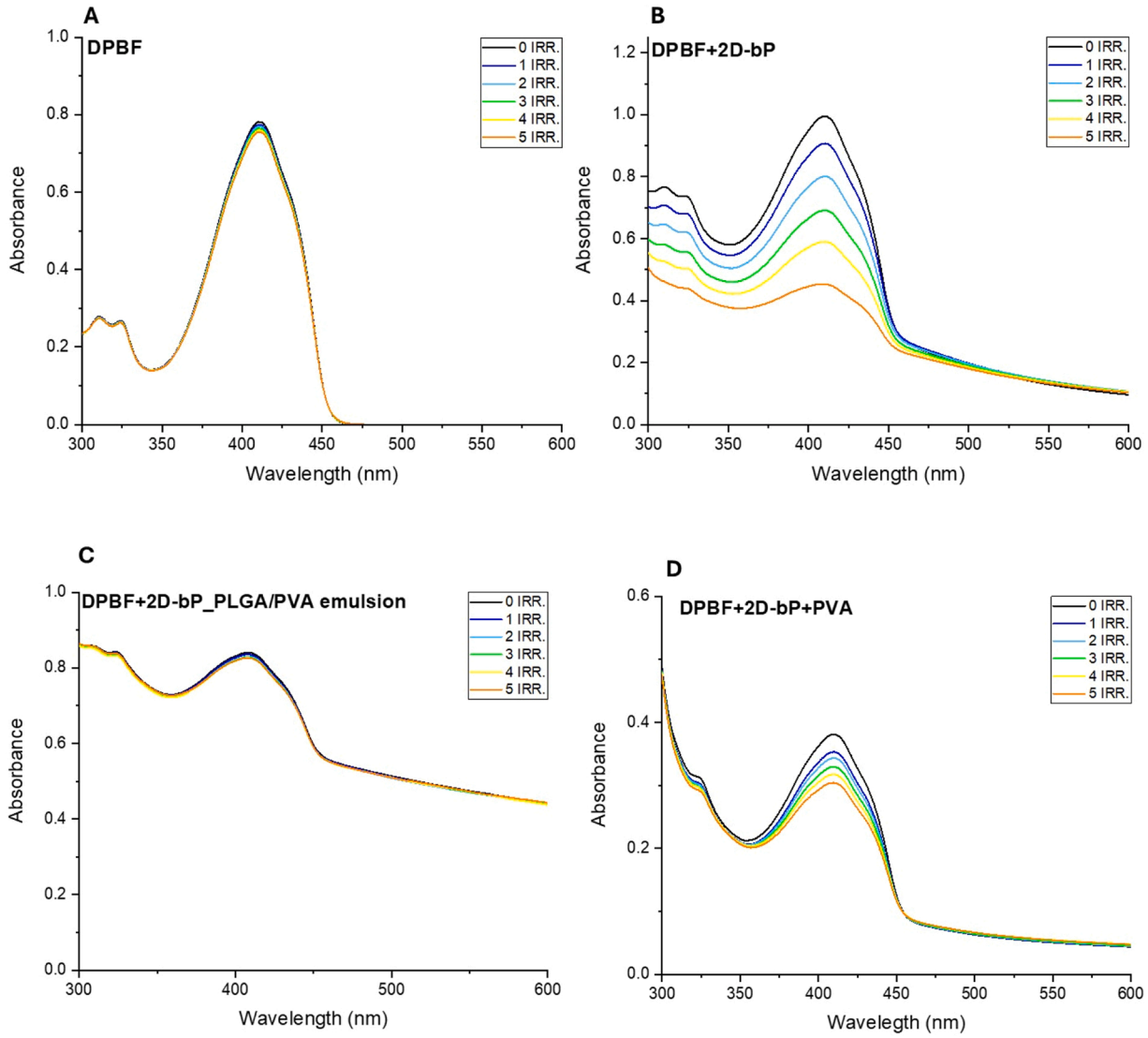

Fig. 8. UV-Vis spectra collected at the beginning of the experiment (0 IRR) and after each irradiation cycle (A) DPBF in ethanol, (B) DPBF in ethanol with 2D-bP suspension, (2D-bP concentration= 0.01 mg/mL, DPBF concentration= 0.02 mg/mL); (C) DPBF in ethanol with 2D-bP_PLGA/PVA emulsion and (D) DPBF in ethanol with 2D-bP suspension +PVA (2D-bP concentration= 0.003 mg/mL, DPBF concentration= 0.006 mg/mL).

Table 2
DPBF reacted and $^1O_2$ produced during each irradiation cycle.

Irradiation cycle	A $_{DPBF}$	C $_{DPBF}$ ($M*10^5$)[a]	mol $_{DPBF}$ present ($mol*10^8$)[b]	mol $_{DPBF}$ reacted ($mol*10^8$)[c]	mol$^1O_2$ produced ($mol*10^8$)[d]
0	0.99	4.30	12.90	-	-
1	0.91	3.96	11.88	1.02	2.04
2	0.80	3.48	10.44	1.44	2.88
3	0.69	3.0	9.0	1.44	2.88
4	0.59	2.57	7.71	1.29	2.58
5	0.45	1.96	5.88	1.83	3.66

[a] calculated as ($A_{DPBF}/\varepsilon_{DPBF}$) $\varepsilon_{DPBF} = 23{,}000\ M^{-1}cm^{-1}$;
[b] calculated as (C_{DPBF}*V), V = 0.003 L);
[c] calculated as (mol $_{DPBF}$ (x irrad. cycle) – mol $_{DPBF}$ (x + 1 irrad. cycle));
[d] mol $_{DPBF}$ reacted = mol $^1O_2$ reacted = 2*(mol $^1O_2$ generated)

polymeric micelles, shielded by the aqueous environment, thus limiting their interaction with the oxygen and DPBF dissolved in solution. This arrangement would restrict their interaction with both dissolved oxygen and DPBF, thereby diminishing the efficiency of $^1O_2$ generation and detection in solution. The slight reduction in the absorbance peak may be attributed to the fact that not all of the 2D-bP is encapsulated within the polymeric micelles because some flakes can likely remain dispersed in the suspension or adhere to the surface of the micelles. Therefore, we can assess that the photoactivity properties of 2D-bP or more precisely, its ability to generate $^1O_2$, actually available for the PDT, are considerably reduced by embedding within the polymer micelles.

It is noteworthy that PVA concentration is remarkable in relation to the amounts of PLGA and 2D-bP, even if lower than the CAC (see experimental part). To confirm that PVA does not significantly impact the reduction of 2D-bP photoactivity in the emulsion system, the same $^1O_2$ generation experiment was conducted using a 2D-bP suspension in water and SDS, with PVA added in the same concentration as present in the emulsion (Fig. 8D). The decrease of the absorbance at 410 nm was evident (~21 %), proving that the presence of PVA in solution does not constitute a particular obstacle to the interaction of 2D-bP with oxygen, confirming that the reduction in photoactivity of the 2D-bP-PLGA/PVA emulsion is primarily due to the encapsulation effect of the polymeric micelles. The fact that there is a minor reduction in the absorbance of the trapper in the presence of PVA (with respect to 2D-bP suspension alone) may be due to a variation in the solubility of oxygen in this solution. In fact, it is reported that PVA has good barrier properties to oxygen in the

solid state [64], but it is possible that, when dissolved in water, it can affect the solubility of the gas in the solution. However, it is evident that significant $^1O_2$ production also occurs when 2D-bP is dispersed in a solution containing PVA, proving that the PLGA embedding of flakes mainly causes the hindering of photoactivity for the emulsion. This encapsulation limits the interaction of the nanomaterial with oxygen. In contrast, PVA, being dissolved in the solution, does not pose a significant barrier to the interaction between 2D-bP and oxygen.

To tentatively restore the photoactivity of 2D-bP embedded flakes, the 2D-bP_PLGA/PVA emulsion was treated with an aqueous solution of NaOH to accelerate the degradation of PLGA micelles, with the sole purpose of facilitating the release of the 2D-bP flakes. After the treatment, the resulting emulsion was tested by irradiation in the presence of DPBF (Fig. 9).

Once again, no decrease in the absorbance of the trapper alone was observed, demonstrating its stability under the experimental conditions used to degrade PLGA micelles. In the case of the emulsion treated with NaOH, we noticed a decrease in the DPBF absorbance of about 8 %. This experimental evidence supports our hypothesis regarding the shielding effect of the PLGA shells on 2D-bP: while the structural stability of 2D-bP is maintained, the PLGA coating may inhibit nanoflakes' photoactivity. By degrading the PLGA shells, the photoactivity of the 2D-bP particles seemed partially reactivated. However, it is important to note the lower photoactivity efficiency compared to pristine nanoparticles (Fig. 8B), likely attributed to the reduced concentration of 2D-bP that was not completely released from the PLGA micelles.

Although PLGA has many advantages as a drug delivery material, its hydrolysis in aqueous and biological environments is slow, particularly in the case of emulsions [65]. Consequently, the release of the active agent can occur over a duration of weeks to months, which may not align with the effective lifespan of certain drugs.

4. Conclusion

2D black phosphorus (2D-bP), exfoliated in aqueous SDS solutions as a greener alternative to toxic, high-boiling organic solvents, was employed to develop novel nanocomposites with PLGA, a biodegradable, bio-based, and biocompatible polymer approved for biomedical use. SDS was found not only to enhance the exfoliation yield but also to stabilize the flakes over time by preventing their aggregation through a surface decoration effect. The hybrid materials were prepared via solution intercalation using 2D-bP flakes of varying concentrations and sizes. Structural and thermal analyses, along with degradation studies, revealed that both the degree of exfoliation and the concentration of 2D-bP influenced the final properties of the composites. Notably, the exfoliated composites displayed enhanced thermal stability above 200 °C, a temperature range in which degradation primarily proceeds via chain scission (cracking). At lower temperatures, however, a slight acceleration in degradation was observed—likely attributable to interactions between the lone electron pairs on 2D-bP and the terminal carbonyl groups of PLGA, which may facilitate the backbiting mechanism. Importantly, 2D-bP had no significant effect on the hydrolytic degradation of PLGA. On the contrary, PLGA exhibited a protective role toward 2D-bP, which remained well preserved within the polymer matrix throughout the hydrolysis process.

Given the established relevance of PLGA micelles as drug delivery carriers, polymer emulsions containing 2D-bP were successfully prepared via an oil-in-water method using PVA as surfactant. Morphological and light scattering analyses confirmed the effective encapsulation of 2D-bP within PLGA micelles. Photoactivity studies demonstrated that 2D-bP suspended in SDS–water exhibited excellent singlet oxygen ($^1O_2$) generation. However, its photoactivity progressively declined with the addition of PVA and was almost completely suppressed following encapsulation within the PLGA micelles. This suppression can be attributed to the barrier properties of the polymer shell, which limit the interactions between 2D-bP, oxygen, and the sensitizer, thereby hindering the generation of reactive oxygen species. Although the hydrolytic degradation of PLGA micelles may allow for partial restoration of photoactivity over time, these findings could be critical in the evaluation of their suitability in biomedical applications, particularly in the context of photodynamic therapy.

CRediT authorship contribution statement

Agata Costanzo: investigation, formal analysis, validation, visualization, methodology, writing-original draft. **Carla Caponio**: investigation, methodology. **Serena Coiai**: supervision, conceptualization, methodology, writing-review & editing. **Francesca Cicogna**: supervision, conceptualization, methodology, writing-review & editing. **Giulia Lorenzetti**: investigation. **Emanuela Pitzalis**: investigation. **Franco Dinelli**: investigation, visualization. **Enrico Berretti**: investigation, visualization. **Stefano Caporali**: investigation, visualization, writing-review & editing. **Andrea Pucci**: supervision, validation, methodology, writing-review & editing. **Elisa Passaglia**: conceptualization,

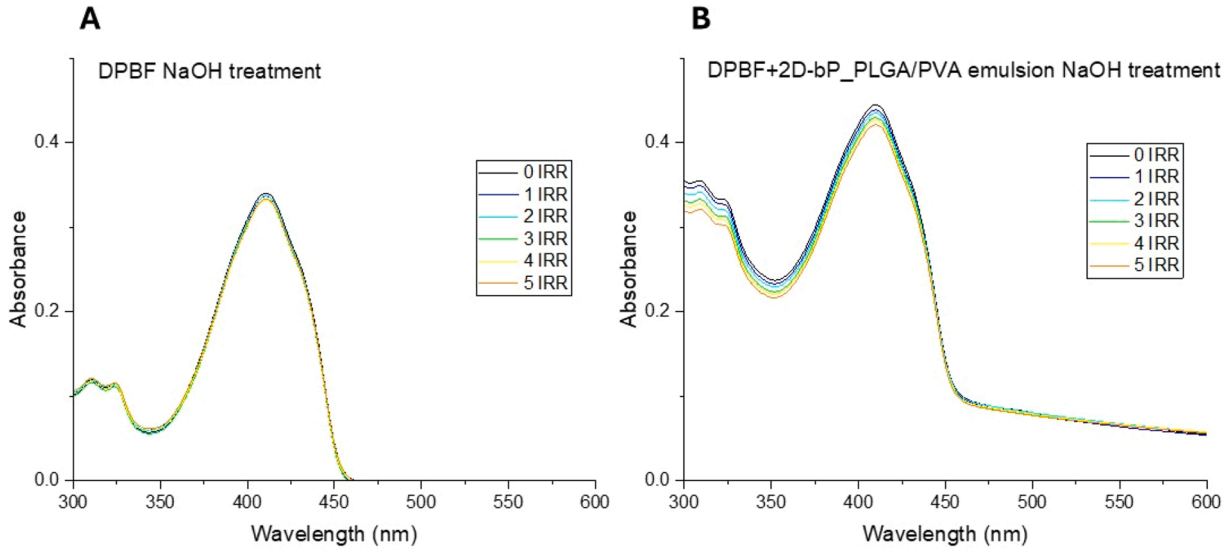

Fig. 9. UV-Vis spectra collected at the beginning of the experiment (0 IRR) and after each irradiation cycle of (A) DPBF in ethanol/water 1/1 vol/vol + 20 mL of NaOH 0.5 M for 3 hrs, (B) DPBF in ethanol/2D-bP_PLGA/PVA emulsion + 20 mL of NaOH 0.5 M for 24 hrs) (DPBF concentration= 0.013 mg/mL).

formal analysis, resources, supervision, validation, visualization, writing-original draft, writing-review & editing.

Declaration of Competing Interest

The authors declare that they have no known competing financial interests or personal relationships that could have appeared to influence the work reported in this paper.

Appendix A. Supporting information

Supplementary data associated with this article can be found in the online version at doi:10.1016/j.nxmate.2025.101529.

Data availability

Data will be made available on request.

References

[1] M. Luo, T. Fan, Y. Zhou, H. Zhang, L. Mei, 2D black phosphorus–based biomedical applications, Adv. Funct. Mater. 29 (2019), https://doi.org/10.1002/adfm.201808306.

[2] M. Tatullo, F. Genovese, E. Aiello, M. Amantea, I. Makeeva, B. Zavan, S. Rengo, L. Fortunato, Phosphorene is the new graphene in biomedical applications, Materials 12 (2019), https://doi.org/10.3390/ma12142301.

[3] X. Liu, B. Gaihre, M.N. George, Y. Li, M. Tilton, M.J. Yaszemski, L. Lu, 2D phosphorene nanosheets, quantum dots, nanoribbons: synthesis and biomedical applications, Biomater. Sci. 9 (2021) 2768–2803, https://doi.org/10.1039/d0bm01972k.

[4] M. Pica, R. D'Amato, Chemistry of phosphorene: synthesis, functionalization and biomedical applications in an update review, Inorganics 8 (2020), https://doi.org/10.3390/inorganics8040029.

[5] L.S. Pires, F.D. Magalhães, A.M. Pinto, New polymeric composites based on two-dimensional nanomaterials for biomedical applications, Polymers 14 (2022), https://doi.org/10.3390/polym14071464.

[6] S. Xiong, X. Chen, Y. Liu, T. Fan, Q. Wang, H. Zhang, T. Chen, Black phosphorus as a versatile nanoplatform: from unique properties to biomedical applications, J. Innov. Opt. Health Sci. 13 (2020), https://doi.org/10.1142/S1793545820300086.

[7] M. Qiu, W.X. Ren, T. Jeong, M. Won, G.Y. Park, D.K. Sang, L.-P. Liu, H. Zhang, J. S. Kim, Omnipotent phosphorene: a next-generation, two-dimensional nanoplatform for multidisciplinary biomedical applications, Chem. Soc. Rev. 47 (2018) 5588–5601, https://doi.org/10.1039/C8CS00342D.

[8] Z. Li, J. Song, H. Yang, Emerging low-dimensional black phosphorus: from physical-optical properties to biomedical applications, Sci. China Chem. (2022), https://doi.org/10.1007/s11426-022-1355-6.

[9] S. Lin, Y. Chui, Y. Li, S.P. Lau, Liquid-phase exfoliation of black phosphorus and its applications, FlatChem 2 (2017) 15–37, https://doi.org/10.1016/j.flatc.2017.03.001.

[10] Y. Zhang, H. Wang, Z. Luo, H.T. Tan, B. Li, S. Sun, Z. Li, Y. Zong, Z.J. Xu, Y. Yang, K.A. Khor, Q. Yan, An air-stable densely packed phosphorene-graphene composite toward advanced lithium storage properties, Adv. Energy Mater. 6 (2016) 1600453, https://doi.org/10.1002/aenm.201600453.

[11] J. Yang, W. Liu, Y. Sun, X. Dong, LVFFARK-PEG-stabilized black phosphorus nanosheets potently inhibit amyloid-β fibrillogenesis, Langmuir 36 (2020) 1804–1812, https://doi.org/10.1021/acs.langmuir.9b03612.

[12] Y. Li, Z. Du, X. Liu, M. Ma, D. Yu, Y. Lu, J. Ren, X. Qu, Near-infrared activated black phosphorus as a nontoxic photo-oxidant for Alzheimer's Amyloid-β peptide, Small 15 (2019) 1901116, https://doi.org/10.1002/smll.201901116.

[13] S. Wang, C. Li, Y. Xia, S. Chen, J. Robert, X. Banquy, R. Huang, W. Qi, Z. He, R. Su, Nontoxic black phosphorus quantum dots inhibit insulin amyloid fibrillation at an ultralow concentration, IScience 23 (2020) 101044, https://doi.org/10.1016/j.isci.2020.101044.

[14] C. Caponio, A. Costanzo, S. Coiai, F. Cicogna, E. Pitzalis, S. Borsacchi, G. Lorenzetti, E. Bramanti, A. Papalini, A. Battisti, A. Sgarbossa, E. Passaglia, Cyrene- and water-based exfoliation of black phosphorus for potential nanolayer-mediated disaggregation of insulin fibrils, FlatChem 45 (2024) 100665, https://doi.org/10.1016/j.flatc.2024.100665.

[15] S.C. Dhanabalan, J.S. Ponraj, Z. Guo, S. Li, Q. Bao, H. Zhang, Emerging trends in phosphorene fabrication towards next generation devices, Adv. Sci. 4 (2017) 1600305, https://doi.org/10.1002/advs.201600305.

[16] A. Rabiei Baboukani, I. Khakpour, V. Drozd, C. Wang, Liquid-based exfoliation of black phosphorus into phosphorene and its application for energy storage devices, Small Struct. 2 (2021) 2000148, https://doi.org/10.1002/sstr.202000148.

[17] L. Chen, G. Zhou, Z. Liu, X. Ma, J. Chen, Z. Zhang, X. Ma, F. Li, H.-M. Cheng, W. Ren, Scalable clean exfoliation of high-quality few-layer black phosphorus for a flexible lithium ion battery, Adv. Mater. 28 (2016) 510–517, https://doi.org/10.1002/adma.201503678.

[18] J. Kumar, M. Shrivastava, First-principles molecular dynamics insight into the atomic level degradation pathway of phosphorene, ACS Omega 7 (2022) 696–704, https://doi.org/10.1021/acsomega.1c05353.

[19] J. Kang, S.A. Wells, J.D. Wood, J.-H. Lee, X. Liu, C.R. Ryder, J. Zhu, J.R. Guest, C. A. Husko, M.C. Hersam, Stable aqueous dispersions of optically and electronically active phosphorene, Proc. Natl. Acad. Sci. 113 (2016) 11688–11693, https://doi.org/10.1073/pnas.1602215113.

[20] J.R. Brent, A.K. Ganguli, V. Kumar, D.J. Lewis, P.D. McNaughter, P. O'Brien, P. Sabherwal, A.A. Tedstone, On the stability of surfactant-stabilised few-layer black phosphorus in aqueous media, RSC Adv. 6 (2016) 86955–86958, https://doi.org/10.1039/C6RA21296D.

[21] USFDA, 21 CFR 172.822 - Sodium lauryl sulfate, (n.d.).

[22] T. Arakawa, T. Niikura, Y. Kita, T. Akuta, Sodium dodecyl sulfate analogs as a potential molecular biology reagent, Curr. Issues Mol. Biol. 46 (2024) 621–633, https://doi.org/10.3390/cimb46010040.

[23] Y. Zhang, C. Ma, J. Xie, H. Ågren, H. Zhang, Black phosphorus/polymers: status and challenges, Adv. Mater. 33 (2021) 1–37, https://doi.org/10.1002/adma.202100113.

[24] P. Gentile, V. Chiono, I. Carmagnola, P. Hatton, An overview of poly(lactic-co-glycolic) acid (PLGA)-based biomaterials for bone tissue engineering, Int. J. Mol. Sci. 15 (2014) 3640–3659, https://doi.org/10.3390/ijms15033640.

[25] S.R. Abulateefeh, Long-acting injectable PLGA/PLA depots for leuprolide acetate: successful translation from bench to clinic, Drug Deliv. Transl. Res. 13 (2023) 520–530, https://doi.org/10.1007/s13346-022-01228-0.

[26] X. Wang, J. Shao, M. Abd El Raouf, H. Xie, H. Huang, H. Wang, P.K. Chu, X.F. Yu, Y. Yang, A.B.M. AbdEl-Aal, N.H.M. Mekkawy, R.J. Miron, Y. Zhang, Near-infrared light-triggered drug delivery system based on black phosphorus for in vivo bone regeneration, Biomaterials 179 (2018) 164–174, https://doi.org/10.1016/j.biomaterials.2018.06.039.

[27] N. Kamyar, R.D. Greenhalgh, T.R.L. Nascimento, E.S. Medeiros, P.D. Matthews, L. P. Nogueira, H.J. Haugen, D.J. Lewis, J.J. Blaker, Exploiting Inherent Instability of 2D black phosphorus for controlled phosphate release from blow-spun poly (lactide- co-glycolide) nanofibers, ACS Appl. Nano Mater. 1 (2018) 4190–4197, https://doi.org/10.1021/acsanm.8b00938.

[28] J. Shao, H. Xie, H. Huang, Z. Li, Z. Sun, Y. Xu, Q. Xiao, X.-F. Yu, Y. Zhao, H. Zhang, H. Wang, P.K. Chu, Biodegradable black phosphorus-based nanospheres for in vivo photothermal cancer therapy, Nat. Commun. 7 (2016) 12967, https://doi.org/10.1038/ncomms12967.

[29] H. Wang, X. Yang, W. Shao, S. Chen, J. Xie, X. Zhang, J. Wang, Y. Xie, Ultrathin black phosphorus nanosheets for efficient singlet oxygen generation, J. Am. Chem. Soc. 137 (2015) 11376–11382, https://doi.org/10.1021/jacs.5b06025.

[30] T. Entradas, S. Waldron, M. Volk, The detection sensitivity of commonly used singlet oxygen probes in aqueous environments, J. Photochem. Photobio. B 204 (2020) 111787, https://doi.org/10.1016/j.jphotobiol.2020.111787.

[31] H. Zakaria, R. El Kurdi, D. Patra, Curcumin-PLGA based nanocapsule for the fluorescence spectroscopic detection of dopamine, RSC Adv. 12 (2022) 28245–28253, https://doi.org/10.1039/D2RA01679F.

[32] Z. Torbatian, R. Asgari, Optical absorption properties of few-layer phosphorene, Phys. Rev. B 98 (2018) 205407, https://doi.org/10.1103/PhysRevB.98.205407.

[33] A.H. Woomer, T.W. Farnsworth, J. Hu, R.A. Wells, C.L. Donley, S.C. Warren, Phosphorene: synthesis, scale-up, and quantitative optical spectroscopy, ACS Nano 9 (2015) 8869–8884, https://doi.org/10.1021/acsnano.5b02599.

[34] M. Akhtar, G. Anderson, R. Zhao, A. Alruqi, J.E. Mroczkowska, G. Sumanasekera, J. B. Jasinski, Recent advances in synthesis, properties, and applications of phosphorene, NPJ 2D Mater. Appl. 1 (2017) 5, https://doi.org/10.1038/s41699-017-0007-5.

[35] A. Kundu, D. Tristant, N. Sheremetyeva, A. Yoshimura, A. Torres Dias, K.S. Hazra, V. Meunier, P. Puech, Reversible pressure-induced partial phase transition in few-layer black phosphorus, Nano Lett. 20 (2020) 5929–5935, https://doi.org/10.1021/acs.nanolett.0c01784.

[36] W. Lu, H. Nan, J. Hong, Y. Chen, C. Zhu, Z. Liang, X. Ma, Z. Ni, C. Jin, Z. Zhang, Plasma-assisted fabrication of monolayer phosphorene and its Raman characterization, Nano Res. 7 (2014) 853–859, https://doi.org/10.1007/s12274-014-0446-7.

[37] J.R. Brent, N. Savjani, E.A. Lewis, S.J. Haigh, D.J. Lewis, P. O'Brien, Production of few-layer phosphorene by liquid exfoliation of black phosphorus, Chem. Commun. 50 (2014) 13338–13341, https://doi.org/10.1039/C4CC05752J.

[38] H. Liu, A.T. Neal, Z. Zhu, Z. Luo, X. Xu, D. Tománek, P.D. Ye, Phosphorene: an Unexplored 2D Semiconductor with a High Hole Mobility, ACS Nano 8 (2014) 4033–4041, https://doi.org/10.1021/nn501226z.

[39] Q. Zhou, Q. Chen, Y. Tong, J. Wang, Light-induced ambient degradation of few-layer black phosphorus: mechanism and protection, Angew. Chem. Int. Ed. 55 (2016) 11437–11441, https://doi.org/10.1002/anie.201605168.

[40] S. Walia, Y. Sabri, T. Ahmed, M.R. Field, R. Ramanathan, A. Arash, S.K. Bhargava, S. Sriram, M. Bhaskaran, V. Bansal, S. Balendhran, Defining the role of humidity in the ambient degradation of few-layer black phosphorus, 2D Mater. 4 (2016) 015025, https://doi.org/10.1088/2053-1583/4/1/015025.

[41] M.C. Zenobi, C.V. Luengo, M.J. Avena, E.H. Rueda, An ATR-FTIR study of different phosphonic acids in aqueous solution, Spectrochim. Acta A Mol. Biomol. Spectrosc. 70 (2008) 270–276, https://doi.org/10.1016/j.saa.2007.07.043.

[42] Y.T. Yew, Z. Sofer, C.C. Mayorga-Martinez, M. Pumera, Black phosphorus nanoparticles as a novel fluorescent sensing platform for nucleic acid detection, Mater. Chem. Front. 1 (2017) 1130–1136, https://doi.org/10.1039/c6qm00341a.

[43] Z. Zhang, X. Wang, R. Zhu, Y. Wang, B. Li, Y. Ma, Y. Yin, Synthesis and characterization of serial random and block-copolymers based on lactide and

glycolide, Polym. Sci. Ser. B 58 (2016) 720–729, https://doi.org/10.1134/S1560090416060191.
[44] K. Yuniarto, Y.A. Purwanto, S. Purwanto, B.A. Welt, H.K. Purwadaria, T.C. Sunarti. Infrared and Raman studies on polylactide acid and polyethylene glycol-400 blend, 2016, 10.1063/1.4945555, 020101.
[45] G. Kister, G. Cassanas, M. Vert, Morphology of poly(glycolic acid) by IR and Raman spectroscopies, Spectrochim. Acta A Mol. Biomol. Spectrosc. 53 (1997) 1399–1403, https://doi.org/10.1016/S0584-8539(97)00039-1.
[46] G. Liu, K. McEnnis, Glass transition temperature of PLGA particles and the influence on drug delivery applications, Polymers 14 (2022) 993, https://doi.org/10.3390/polym14050993.
[47] M. Ayyoob, Y. Kim, Effect of chemical composition variant and oxygen plasma treatments on the wettability of PLGA thin films, synthesized by direct copolycondensation, Polymers 10 (2018) 1132, https://doi.org/10.3390/polym10101132.
[48] J. Palacios, C. Albano, G. González, R.V. Castillo, A. Karam, M. Covis, Characterization and thermal degradation of poly(D,L-lactide- co -glycolide) composites with nanofillers, Polym. Eng. Sci. 53 (2013) 1414–1429, https://doi.org/10.1002/pen.23396.
[49] Y. Zhang, J. Wang, Q. Liu, S. Gu, Z. Sun, P.K. Chu, X. Yu, The electrical, thermal, and thermoelectric properties of black phosphorus, APL Mater. 8 (2020), https://doi.org/10.1063/5.0027244.
[50] E. Passaglia, F. Cicogna, G. Lorenzetti, S. Legnaioli, M. Caporali, M. Serrano-Ruiz, A. Ienco, M. Peruzzini, Novel polystyrene-based nanocomposites by phosphorene dispersion, RSC Adv. 6 (2016) 53777–53783, https://doi.org/10.1039/c6ra10133j.
[51] R. Mouhoubi, M. Lasschuijt, S. Ramon Carrasco, H. Gojzewski, F.R. Wurm, End-of-life biodegradation? how to assess the composting of polyesters in the lab and the field, Waste Manag. 154 (2022) 36–48, https://doi.org/10.1016/j.wasman.2022.09.025.
[52] M.F. Silva, A.A.W. Hechenleitner, J.M. Irache, A.J.A. de Oliveira, E.A.G. Pineda, Study of thermal degradation of PLGA, PLGA nanospheres and PLGA/maghemite superparamagnetic nanospheres, Mater. Res. 18 (2015) 1400–1406, https://doi.org/10.1590/1516-1439.045415.
[53] J. Parikh, A. Raval, Review on hydrolytic degradation behavior of biodegradable polymers from controlled drug delivery system, Trends Biomater. Artif. Organs 25 (2011) 79–85.
[54] R. Machatschek, A. Lendlein, Fundamental insights in PLGA degradation from thin film studies, J. Control. Release 319 (2020) 276–284, https://doi.org/10.1016/j.jconrel.2019.12.044.
[55] C. Martins, F. Sousa, F. Araújo, B. Sarmento, Functionalizing PLGA and PLGA derivatives for drug delivery and tissue regeneration applications, Adv. Health Mater. 7 (2018), https://doi.org/10.1002/adhm.201701035.
[56] H. Zakaria, R. El Kurdi, D. Patra, A novel study on the self-assembly behavior of poly(lactic- co -glycolic acid) polymer probed by curcumin fluorescence, ACS Omega 7 (2022) 9551–9558, https://doi.org/10.1021/acsomega.1c06919.
[57] C. Albert, N. Huang, N. Tsapis, S. Geiger, V. Rosilio, G. Mekhloufi, D. Chapron, B. Robin, M. Beladjine, V. Nicolas, E. Fattal, F. Agnely, Bare and sterically stabilized PLGA nanoparticles for the stabilization of pickering emulsions, Langmuir 34 (2018) 13935–13945, https://doi.org/10.1021/acs.langmuir.8b02558.
[58] D. Xu, J. Liu, Y. Wang, Y. Jian, W. Wu, R. Lv, Black phosphorus nanosheet with high thermal conversion efficiency for photodynamic/photothermal/immunotherapy, ACS Biomater. Sci. Eng. 6 (2020) 4940–4948, https://doi.org/10.1021/acsbiomaterials.0c00984.
[59] E. Passaglia, A. Sgarbossa, Innovative phosphorene nanoplatform for light antimicrobial therapy, Pharmaceutics 15 (2023) 2748, https://doi.org/10.3390/pharmaceutics15122748.
[60] Z. Wei, W. Li, Z. Liu, Y. Zhu, H. Cao, Hydrogen bond-bridged phosphorene flexible film for photodynamic inhibiting Staphylococcus aureus, Nano Res. 17 (2024) 5461–5468, https://doi.org/10.1007/s12274-024-6487-7.
[61] W. Liu, Y. Zhang, Y. Zhang, A. Dong, Black phosphorus nanosheets counteract bacteria without causing antibiotic resistance, Chem. A Eur. J. 26 (2020) 2478–2485, https://doi.org/10.1002/chem.201905134.
[62] J.R. Choi, K.W. Yong, J.Y. Choi, A. Nilghaz, Y. Lin, J. Xu, X. Lu, Black phosphorus and its biomedical applications, Theranostics 8 (2018) 1005–1026, https://doi.org/10.7150/thno.22573.
[63] M.A. Murcia Valderrama, R.-J. van Putten, G.-J.M. Gruter, PLGA barrier materials from CO $_2$. The influence of lactide co-monomer on glycolic acid polyesters, ACS Appl. Polym. Mater. 2 (2020) 2706–2718, https://doi.org/10.1021/acsapm.0c00315.
[64] M. Lim, H. Kwon, D. Kim, J. Seo, H. Han, S.B. Khan, Highly-enhanced water resistant and oxygen barrier properties of cross-linked poly(vinyl alcohol) hybrid films for packaging applications, Prog. Org. Coat. 85 (2015) 68–75, https://doi.org/10.1016/j.porgcoat.2015.03.005.
[65] R.L. McCall, R.W. Sirianni, PLGA nanoparticles formed by single- or double-emulsion with vitamin E-TPGS, J. Vis. Exp. (2013), https://doi.org/10.3791/51015.